



Montanuniversität Leoben

Lehrstuhl für Allgemeinen Maschinenbau (AMB)

Franz-Josef-Straße 18

A-8700 Leoben – Austria



Master's Thesis

NUMERICAL SENSITIVITY STUDY OF RESIDUAL STRESS AND DISTORTION IN SELECTIVE LASER MELTING OF 17-4 PH STEEL

created at the

Montanuniversität Leoben

Chair of Mechanical Engineering

Submitted by:

Albert Martínez Bastús, Bsc

Supervisors:

Univ.-Prof. Dr. Florian Grün

Ass.Prof. Dr. Martin Leitner, MBA

Leoben, July 2019

Acknowledgements

Firstly, I would like to thank my master's thesis supervisor and head of the Mechanical Engineering Department of the Montanuniversität Leoben Univ.-Prof. Dr. Florian Grün for giving me the chance to conduct my thesis in one of the projects in which the department is involved and whose topic I think will be very important in the future. I am also truly thankful to my co-supervisor Ass.Prof. Dr. Martin Leitner, MBA for its support, supervision, guidance and advices which steered me in the right direction during the development of this thesis.

I would like to thank Bsc. Florian Beter for giving me advices of how to use Simufact Additive. Its help and the conversations we have had during my stay in Leoben have been really useful to investigate and to have a deep understanding of the simulation software and selective laser melting. I also thank him for testing the specimens.

I give my very profound gratitude to my beloved ones specially my parents, my brother and my aunt for its unfailing support during my stay abroad despite the distance and also for visiting me in Austria. I am forever indebted to my parents for giving me the opportunity to study abroad. I also specially want to thank Clarissa for encouraging me to study abroad, supporting me during my hardest moments and make this 2 last year's special. They all have been my strength.

Finally, I would like to thank Montanuniversität Leoben and UPC-ETSEIB for making this thesis and Erasmus exchange possible. Thank you very much.

Abstract

Additive manufacturing is shaping the future of part production by making possible to create any part with complex geometry and ease product development stages. Selective laser melting, which is one type of additive manufacturing capable of melting metal powders by using a high energy laser beam, has increased the interest to many companies due to its potential for industrial applications. However, there is still research needed in order to improve its mechanical properties. In these cases, Computer aided engineering software is used to predict the mechanical properties before manufacturing and save costs. In this project a sensitivity study using Simufact Additive software was performed with the aim predicting the effect of the process parameters and heat treatment in the residual stresses and distortion on 17-4 PH stainless steel. Before performing the sensitivity study, a voxel mesh study of one specimen was performed to find the optimal element size. In addition, more material data was added to enable heat treatment and improve the accuracy of the simulation. Finally, the sensitivity study was performed and the results were compared to specimens measured via X-ray diffraction. As a remarkable outcome, it was found that heat input parameters have a relation with the tensile residual stresses and distortion. The residual stress and distortion were found to follow the same rule as welding process and the pattern of the residual stress distribution found was equal to others scientific research in the field.

Contents

LIST OF FIGURES	VII
LIST OF TABLES	X
1 INTRODUCTION	1
1.1 Motivation	1
1.2 Objectives	2
2 STATE OF THE ART	3
2.1 Additive Manufacturing	3
2.1 Selective Laser Melting	3
2.1.1 Process	3
2.1.2 Manufacturing parameters	4
2.2 Distortion	7
2.3 Residual stress	8
2.3.1 Classification	8
2.3.2 Mechanisms of formation	9
2.3.3 Influence of machine parameters in residual stress	11
2.3.4 Reduction of residual stress in AM	12
2.4 17-4 PH	13
2.5 Simulation of AM process	15
2.5.1 Macroscale simulation	16
3 METHODOLOGY	21
4 RESIDUAL STRESS MEASUREMENTS	22
5 SINGLE SPECIMEN	23
5.1 Procedure	23
5.1.1 New material added	24
5.2 Results	27
5.2.1 Voxel mesh study	27
5.2.2 Default data vs new data	28
5.3 Discussion	33
6 SENSITIVITY STUDY	35
6.1 Procedure	35
6.1 Results	37
6.1.1 Residual Stresses	37
6.1.2 Distortion	53

6.2 Discussion.....	63
CONCLUSIONS	65
BIBLIOGRAPHY	67

List of figures

Fig. 2.1: Machine description [1]	4
Fig. 2.2: Process window for an iron based powder mixture [13]	6
Fig. 2.3: Different scan strategies [15]	7
Fig. 2.4: Relation between residual stress and distortion in welding process[14]	8
Fig. 2.5: Distribution of residual stresses according to its types and scales.[17]	9
Fig. 2.6: Thermal mechanism of residual stress during heating (a) and cooling (b)[15]	10
Fig. 2.7: Plane direction residual stresses vs different power and scanning speed applied in a top layer plane[21]	11
Fig. 2.8: Precipitation hardening process[25]	14
Fig. 3.1: Specimen design	21
Fig. 5.1: New flow curves at $0,001 \text{ s}^{-1}$ strain rate added	24
Fig. 5.2: Thermal conductivity at different temperatures: data added vs default	25
Fig. 5.3: Young's Modulus at different temperatures: data added vs default	25
Fig. 5.4: Thermal expansion coefficient at different temperatures: data added vs default	26
Fig. 5.5: Residual stress and distortion at different voxel sizes	27
Fig. 5.6: Residual stress and exposure energy fraction at different voxel sizes	27
Fig. 5.7 Single specimen residual σ_z with data by default	28
Fig. 5.8: Single specimen residual σ_z with new data added without heat treatment	29
Fig. 5.9: Single specimen residual σ_z with new data added and heat treatment	29
Fig. 5.10: Boxplot single specimen residual σ_z with new material data added accumulatively in the measured section	30
Fig. 5.11: Single specimen residual σ_z average with new material data added accumulatively in the measured section	30
Fig. 5.12: Single specimen distortion with data by default	31
Fig. 5.13: Single specimen distortion with new material data added without heat treatment	32

Fig. 5.14: Single specimen distortion with new material data with heat treatment	32
Fig. 5.15: Single specimen maximum and minimum distortion with new material data added	33
Fig. 6.1: Specimen building layout with numbering and dimensions	35
Fig. 6.2: Residual stress simulation with default material data	37
Fig. 6.3: Residual stress simulation with new material data without heat treatment	38
Fig. 6.4: Residual stress simulation with new material data and heat treatment.....	38
Fig. 6.5: Boxplot of residual σ_z at E8-S6-B5	40
Fig. 6.6: Boxplot of residual σ_z at E8-S6-B1	40
Fig. 6.7: Boxplot of residual σ_z at E8-S7-B5	41
Fig. 6.8: Boxplot of residual σ_z at E8-S7-B1	41
Fig. 6.9: Boxplot of residual σ_z at E8-S8-B5	42
Fig. 6.10: Boxplot of residual σ_z at E8-S8-B1	42
Fig. 6.11: Boxplot of residual σ_z at E9-S6-B5	43
Fig. 6.12: Boxplot of residual σ_z at E9-S6-B1	43
Fig. 6.13: Boxplot of residual σ_z at E9-S7-B5	44
Fig. 6.14: Boxplot of residual σ_z at E9-S7-B1	44
Fig. 6.15: Boxplot of residual σ_z at E9-S8-B5	45
Fig. 6.16: Boxplot of residual σ_z at E9-S8-B1	45
Fig. 6.17: Boxplot of residual σ_z at E1-S6-B5	46
Fig. 6.18: Boxplot of residual σ_z at E1-S6-B1	46
Fig. 6.19: Boxplot of residual σ_z at E1-S7-B5	47
Fig. 6.20: Boxplot of residual σ_z at E1-S7-B1	47
Fig. 6.21: Boxplot of residual σ_z at E1-S8-B5	48
Fig. 6.22: Boxplot of residual σ_z at E1-S8-B1	48

Fig. 6.23: Efficiency, scanning speed and beam width effect in residual stress	49
Fig. 6.24: General factorial regression of residual stress with MINITAB	50
Fig. 6.25: Residual plots of the residual stress regression	51
Fig. 6.26: Effects of individual parameters on residual stress	51
Fig. 6.27: Residual σ_z vs scan rate	52
Fig. 6.28: Residual σ_z vs energy density	52
Fig. 6.29: Residual σ_z correlation test with scan rate and energy density	52
Fig. 6.30: Residual σ_z correlation test with scan rate and energy density after removing biased points	53
Fig. 6.31: Distortion in specimens with default data.....	53
Fig. 6.32: Distortion in specimens with new data and without heat treatment	54
Fig. 6.33: Distortion in specimens with new data and heat treatment	54
Fig. 6.34: Evolution of maximum and minimum distortion average with material data added	55
Fig. 6.35: Max and Min distortion vs scanning speed and efficiency at 50 μm beam width	56
Fig. 6.36: Max and Min distortion vs scanning speed and efficiency at 100 μm beam width	57
Fig. 6.37: General regression of Maximum distortion with MINITAB.....	58
Fig. 6.38: Residual plots of maximum distortion regression	59
Fig. 6.39: Effects of individual parameters in maximum distortion	59
Fig. 6.40: General regression of Minimum distortion with MINITAB.....	60
Fig. 6.41: Residual plots of the minimum distortion regression	61
Fig. 6.42: Effects of individual parameters in minimum distortion	61
Fig. 6.43: Maximum and minimum distortion vs energy density.....	62
Fig. 6.44: Maximum and minimum distortion vs scan rate	62
Fig. 6.45: Correlation test of minimum distortion vs energy density and scan rate	63

List of tables

Table 2.1 Chemical composition of 17-4 PH (%) according to EN 14542	13
Table 4.1: Residual σ_z results of the measurements	22
Table 6.1: Residual stress sensitivity study results table	39
Table 6.2: max and min distortion sensitivity study results table	56

1 Introduction

1.1 Motivation

Additive manufacturing is currently carrying a new industrial revolution by being able to produce complex geometry parts without using any mould or die and it is believed that will substitute other classical manufacturing processes like casting or injection moulding because the product development phase is faster and cheaper (no need of development extra tooling). Automotive, aeronautical and medical industry are driving its interests in metal additive manufacturing because of its strength, versatility and heat resistance compared to plastic. As a result, these days we can find some manufacturing companies that are starting to use additive manufacturing to produce metal parts in small batches. One of the most used metal additive manufacturing process is selective laser melting.

Unfortunately, right now the final mechanical properties of metal parts are not as good as they desired and this topic is one of the main fields of research in additive manufacturing. Two of the main mechanical properties related to additive manufacturing of materials are distortion and residual stresses. Distortions can result in non-desired geometry and tolerances and residual stresses can lead to premature failure or less mechanical strength.

The chair of mechanical engineering of Montanuniversität Leoben is now researching residual stresses and part distortion in metal additive manufacturing. To conduct this research, they have CAE software for numerical simulations and testing available in their department. One of this CAE software is Simufact Additive which has proved to be really helpful to predict part distortion and residual stresses.

Previously to this project, the chair of mechanical engineering of Montanuniversität Leoben has been researching about welding processes and there are resemblances between these two processes. Regarding selective laser melting, the purpose is to understand how the different process parameters affect residual stress and distortion and try to find the best configuration parameters that can lead to reduce part distortion and residual stresses. In addition, another purpose is to understand how Simufact Additive works. Nowadays they have ordered additive manufactured specimens made of AlSi10Mg, TiAl6V4 and 17-4 PH powder to conduct the research.

1.2 Objectives

This project is intended to use Simufact Additive software to simulate selective laser melting of 17-4 PH. The main goals of this project are the following:

- Simulate the real manufacturing conditions of the specimens and compare them with the real results.
- Perform a sensitivity study on the residual stress and distortion of 17-4 PH:
 - Find the best parameter configuration based on the simulation results obtained.
 - Establish a relation between the manufacturing parameters and its residual stress and distortion and compare it with other scientific research.

2 State of the art

2.1 Additive Manufacturing

Additive Manufacturing (AM), also known as 3D printing, is a manufacturing process that builds 3D parts by adding material progressively layer-by-layer. In order to manufacture parts, CAD data is needed and then the machine divides the file into various layers that will be created during the building process. Once the part is completely built, it is removed from the machine.

This manufactured method is opposed to subtractive methods because it is based on adding material and it is different from other manufacturing conventional methods such as forging, injection, casting and sintering because there is no extra tooling (e.g mould or die) apart from the machine used. Over the years this manufacturing process has become more important, in the beginning its main use was in Rapid Prototyping because for small batches is cheaper and its product development stage is fast but nowadays, we can find a lot of medical, automotive, aeronautic and customized applications due to its technology improvement. Although AM is gaining importance, there is further research needed in order to improve the produced parts quality and its manufacturing cycle time.

2.1 Selective Laser Melting

2.1.1 Process

Selective Laser Melting (SLM) is an AM method based in melting metal powder in a powder-based bed. This process consists in a laser beam that selectively heats and melts certain areas of a layer from the powder bed. Once the selected parts of the layer are heated and melted a new layer is added. A detailed description of the process and a sketch of the main components of the machine is found below (Fig. 2.1):

1. Powder Layer Deposition. A metal powder layer from a hopper or feed container is laid to a substrate platform (building plate) by means of a recoater that spreads the powder and gives a uniform distribution over the building plate. This layer has a typical thickness between 20-100 μm [1], [2]. In addition to this, the building plate can be preheated between 200-500 °C which allows to lower the thermal gradient and this means that distortions are reduced and hence residual stress of the final part[3].

2. **Selective Laser Melting.** A laser beam with a power between 20W and 1kW [2][4] scans selectively areas of the added layer with a scanning speed up to 15 m/s[1]. These areas are heated and melted and while they are melted a rapid cooling process is applied. At the end the desired powder particles are united. All this process is done in a chamber with an inert gas (Argon or Nitrogen) in order to protect the metal powder from oxidation. The heating/cooling rates are between 10^3 and 10^8 K/s.[5]
3. **Build Plate Lowering.** Once all the selected areas become solid, the plate lowers and a new layer is added to the substrate.

Then the Powder Layer Deposition, the Selective Laser Melting and the Build Plate Lowering steps are done again until the desired part is done.

4. **Part and Powder Removal.** The powder non-melted is removed from the building plate and the final part is revealed. Finally, the part is cut from the building plate and the process is finished.

After all this process a post process treatment can be applied to the part to improve its mechanical properties.

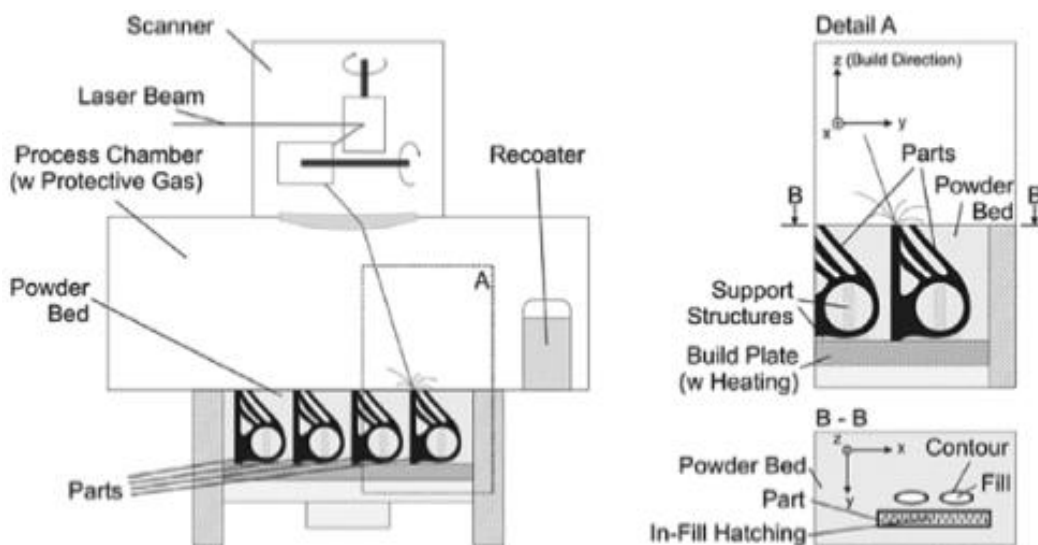


Fig. 2.1: Machine description [1]

2.1.2 Manufacturing parameters

To get a good quality part there are several process parameters/factors to take into account, some of them depend on the machine, others not and have to be chosen carefully in order to fabricate a defect-free part. Research shows that depending on the value of the parameters/factors chosen, the mechanical properties of the part will be different [2]. A description of the used parameters in SLM manufacturing can be the following:

- **Laser Power.** Energy per second that the laser applies to the powder bed. This energy makes the material to heat up and melt. When the power given is too high the material will be melted in excess or even evaporated and when the power is too low the material might not be melted hence no part will be manufactured. Apart from this, depending of the material used the manufacturer has to take into account that not all the energy applied is absorbed by the powder, there is the absorptance of the material which is defined as the rate of energy absorbed by the material vs the total energy applied.
- **Hatch Spacing,** defined as the distance between the central line of two neighbouring paths scanned. This distance can be controlled by the machine. If the hatching spacing is too big, the adjacent scanned paths won't be joined together which means that scanned paths will have a weak boundary between them and the mechanical resistance from the manufactured part would be lower. Nevertheless, a low hatch spacing might give a lot of energy to the scanned areas and this might evaporate or give more temperature to the previous scanned paths.
- **Scanning Speed,** it defines how fast the laser scanner moves while scanning. High speed scanning results in poor energy given to the scanned path and it might not be melted at all. In addition, low scanning speed can lead to too much energy applied to the scanned path and therefore too much temperature in the powder than can result in non-desired melted areas.
- **Layer thickness.** The new layer height added to the powder bed once the selective laser melting step is finished. The literature shows that the lower the powder thickness is, the better dimensional and the denser the 3D printed parts will be. In addition, its Young's Modulus, ultimate tensile strength, yield tensile strength and hardness are also better when the layer thickness is the small as possible[6][7]. Nevertheless, reducing its layer thickness means that more layers need to be added to the model and therefore it increases the cycle time.
- **Energy density.** All the parameters mentioned before interact between them. When the scanning speed is low and the laser power is high too much energy is applied to the selected area increasing its temperature and thermal stress during the solidification process. However, when the scanning speed is high and the laser power is low the energy input is not enough to melt the desired path. Hatch spacing and layer thickness have an effect during the heat transfer process: the more layer thickness the more thermal conduction resistance will be and the different hatch spacing create a different temperature distribution over the scanned paths. Energy density pretends to be the average energy applied per volume and is defined as the following Eq.(1):

$$E = \frac{P}{v \cdot h \cdot d} \quad (1)$$

Where E is energy density (J/mm³), P is laser Power (W), v is scanning speed (mm/s), d is hatching distance (mm) and h Layer thickness (mm). Notice that this equation it is not a true measurement of the real energy density applied to the material, it is just an estimation that does not take into consideration the beam heat profile and its size. In addition to this it is also known that the laser heat profile also penetrates the layer size and affects the underlying layers. The product of the denominator is also known as Scan rate (\dot{V}) Eq.(2):

$$\dot{V} = v \cdot h \cdot d \quad (2)$$

Although energy density parameter is widely used in SLM process [8][9] and remarked as useful to improve and understand the mechanical properties of the material and reduce its defects, some papers indicate that it is not a reliable parameter at all [10][11][12]. Therefore, the right choice of parameters is usually particularized in every case. A process window is used to map the best parameters configuration that lead to avoid defects or improve its mechanical properties (Fig. 2.2).

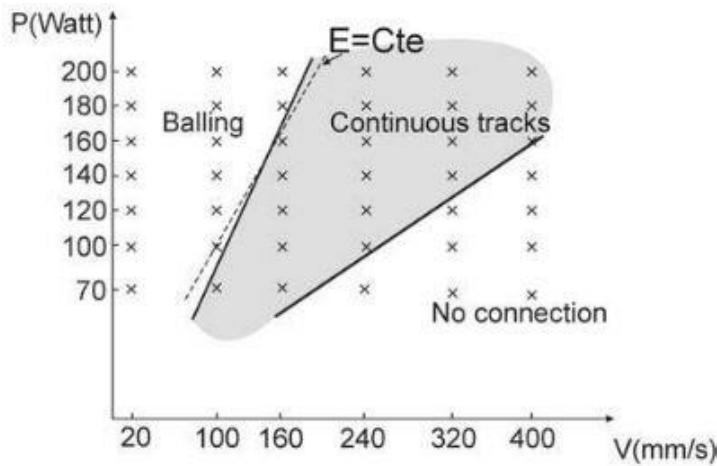


Fig. 2.2: Process window for an iron based powder mixture [13]

- Scan strategy (Hatching strategy). We can define scan strategy as the trajectory the laser beam applies heat during a layer forming. This parameter has a big impact in the anisotropy because every layer is made of scanned tracks and it is obvious that the boundary between particles of different scanned tracks is not as strong as the boundary between particles of scanned tracks. In the literature we can find different scan strategies (Fig. 2.3): straight unidirectional lines, straight alternate direction lines, checker board strategies (also known as island strategies), spiral etc. Sometimes these strategies are alternated in different layers of the same part.

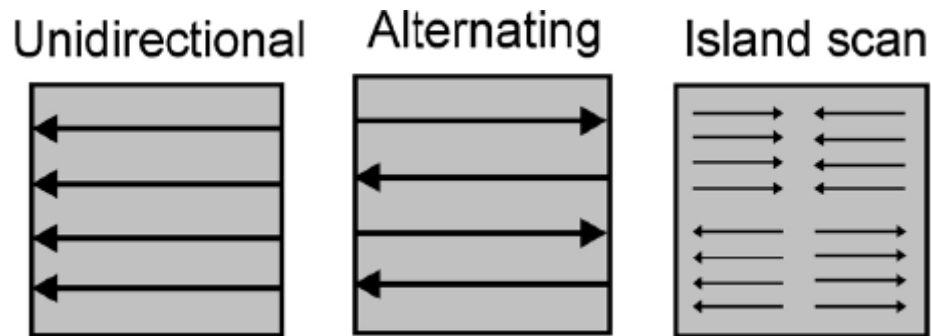


Fig. 2.3: Different scan strategies [15]

2.2 Distortion

Distortion in AM is the geometry difference between the CAD file dimensions introduced into the machine and the resulting manufactured part. In AM this defect comes from the expansion and contraction of the material due to the heat applied and the high cooling rates and the unequal heat conduction of the part. When the heat source applies energy to the layer, the layer increases its temperature and therefore its volume. In the rapid cooling stage, the melted material attempts to contract and recover the original shape it would have occupied in a lower temperature, but it is restrained from doing it by the underlying layer. When the underlying layer prevents the new built layer from recovering its original situation, tensions arise and if they reach the yield strength, a plastic strain is induced resulting in distortion (and also residual stresses). In welding process this effect is related to residual stress. The relation between them is illustrated in Fig. 2.4. When the distortion increases residual stresses decrease, the opposite way is also true.

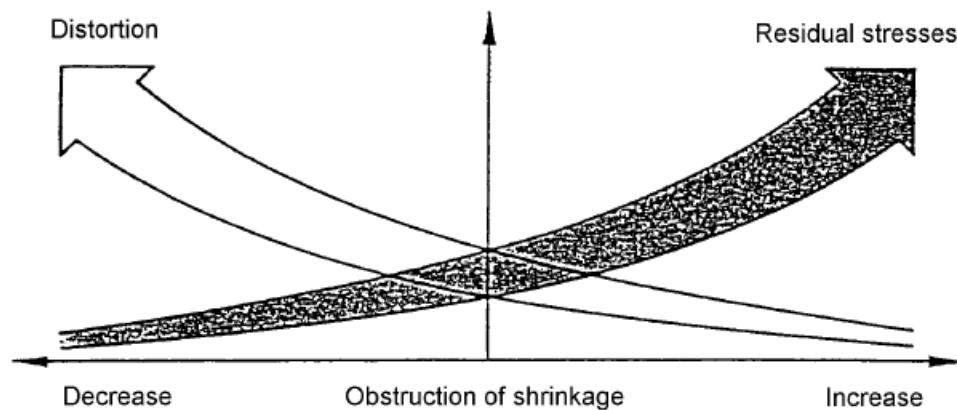


Fig. 2.4: Relation between residual stress and distortion in welding process[14]

2.3 Residual stress

Residual stresses can be defined as “stresses which remain in a material at equilibrium without external loads applied after manufacturing, heating, or other alterations that results in a material undergoing in a non-uniform plastic deformation”[15]. These stresses are often unintentionally introduced during fabrication and they must be taken into account. There can be in the same part compression residual stresses or traction residual stresses and its value depending on the orientation and order of magnitude can be beneficial or detrimental. If there are traction stresses applied to a zone where there are compressive residual stresses, the total traction stress will be less than the external stress applied. In addition to this, the opposite situation can also be done where the total applied stress is bigger than the expected (residual stress and applied stress have the same direction) and hence the part will collapse before than expected. Something similar happens with fatigue cycles but in this case the average stress value and the stress amplitude are changed, modifying its fatigue resistance.

2.3.1 Classification

Residual stresses can be classified into three groups according to the scale in which they operate[16]:

- Type I: Macro stresses. They are in macroscale and they involve large distances, they vary continuously along the part length. They can result in big part deformations and they appear due to a non-uniform plastic deformation in grand scale.

- Type II: Granular stresses. These stresses change over the grain scale. They appear for two main reasons: one is due to the fact that thermomechanical properties change depending on the orientation (anisotropy). The other reason, and with more significant impact, is due to different phases and phase changes transition in the microstructure because of the mechanical properties of the phases.
- Type III: Molecular stresses. These stresses are originated due to the different molecular structure and its dislocation stress fields.

Type II and type III are also known together as microstresses. When it is about measuring, the available techniques can measure different values because of its resolution and the appearance of the different residual types. The following picture illustrates the different issues while measuring (Fig. 2.5). Whereas a multi-phase material has a continuous macrostress profile, type II and type III are not continuous. This fact is because of the sampling volume and its resolution, which include or not whole grains/molecules. In an overall grain/molecular measurement the residual stress is zero. For the macrostresses measurement, an overall measurement of the part also shows zero residual stress, because no loads are applied and as a result it is under equilibrium conditions.

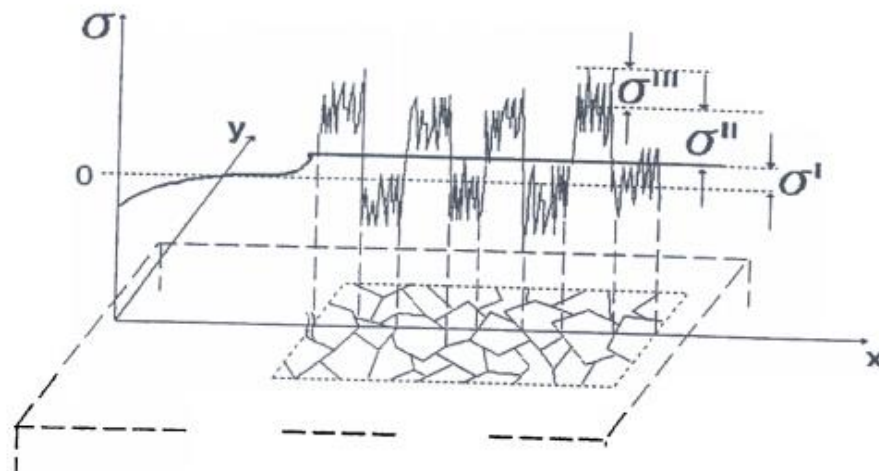


Fig. 2.5: Distribution of residual stresses according to its types and scales.[17]

2.3.2 Mechanisms of formation

Regarding the mechanism of formation, there are three types[17]:

- Due to mechanical stresses. For example, consider the case of a metal bar bent experiencing a plastic deformation. Once the applied force is removed, the bend zone areas will try to recover its original state but the adjacent areas to the bend have

undergone to elastic stress only and they will return to its original position. Therefore, there is a mismatch between the areas experiencing a plastic deformation and the ones who only undergo to elastic deformation. As a result, a residual stress will appear in the area in order to balance the situation. In additive manufacturing this mechanism barely exists, we can only find a reduction of mechanical stresses in the stage of removing the parts from the base plate[18].

- Due to a temperature gradient. This mechanism is commonly known for AM processes and also welding processes[18]. In AM case, the residual stresses are created due to the rapid heating of the upper surface, followed by slow heat conduction. As a result, a steep temperature gradient develops. Due to the steep temperature gradient, the heated zone expansion is bigger than the not heated one and it will be restricted by the underlying cooled layers, then compressive stresses are induced to the new layer and traction stresses are induced to the previous layer. At high temperature the yield strength is lower and the tensile stresses can overcome it, then the area undergoes to plastic deformation (Fig. 2.6 a).

In the cooling stage (no heat source applied), the formed zone starts to shrink and it is partially restrained by underlying layers and the plastic strain zone formed during the heating stage. Finally, the new layer added gets tensile stresses due to the previous layers and to compensate compressive residual stresses are induced to the underlying layers. (Fig. 2.6 b)

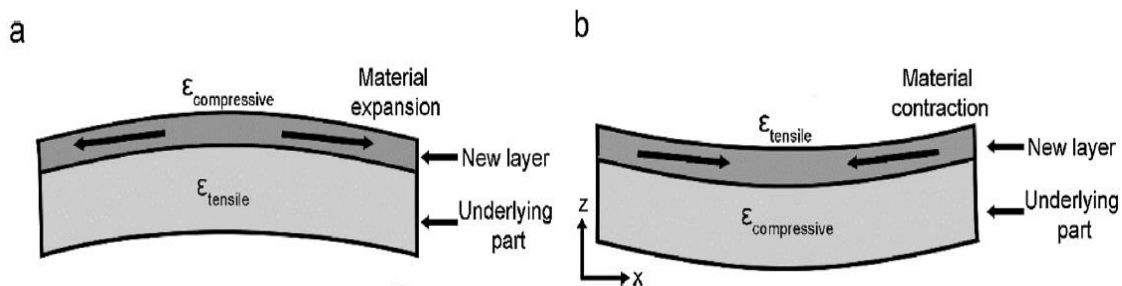


Fig. 2.6: Thermal mechanism of residual stress during heating (a) and cooling (b)[15]

Nevertheless, this example is only helpful to understand the mechanism of residual stress formation. In a real AM process the residual stress field is more complicated due to the nonlinear material properties that change along temperature and the heat profile applied[19]. However, many investigations have showed a residual stress distribution pattern along the building direction. Research confirm that the top and the bottom layer are normally in tensile stress, while intermediate layers experience compressive stress. This fact has been proven also in finite element models and experiments[15].

- Due to chemical generated stresses. Chemical residual stresses are developed because of volume changes related to phase changes, precipitation formation or chemical reactions as well.

2.3.3 Influence of machine parameters in residual stress

In the literature lots of studies have performed experimental measurements in order to estimate the impact of process parameters on the residual stress. In this section a short review of the parameters influence on residual stress is showed. As a remarkable fact, some authors point that processing parameters have bigger impact than in residual stress than material properties[20].

Regarding the influence of scan speed and power, there is a big interaction between those parameters. While some researches show that the higher the power, the more residual stress is induced other investigations point out that the higher scanning speed, the less residual stress induced[21]. As it has been seen in other sections both parameters are important in the so-called energy density parameter: low power applied and high scanning speed mean low energy density and therefore the residual stress should be low. This fact is also pointed out in research (Fig. 2.7) [15][21][22]. Nevertheless, as it has been said in others sections of this document energy density it is not the true real energy density applied (Section 2.1.2) so further research should be done in that topic. Same effects regarding energy density were found in thermomechanical simulations[15].

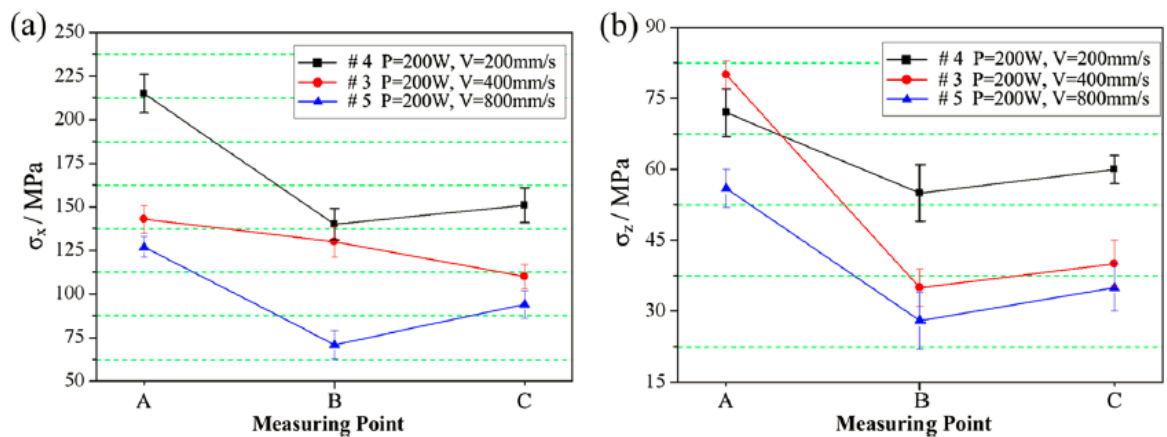


Fig. 2.7: Plane direction residual stresses vs different power and scanning speed applied in a top layer plane[21]

The layer thickness should also play an important role in residual stress. By adding more layer thickness, the temperature difference between the external layer surface and the layer surface

in contact to the built-part should be bigger thus less temperature gradient in the built part and less residual stress induced. Previous research show that residual stresses are reduced by increasing the layer thickness[23].

Regarding the effect of the different scanning strategies, no differences regarding residual stresses were found by applying unidirectional scanning or alternating scanning [24], but it was found that the larger the scanned path the higher residual stress was obtained. In addition, alternating different scanning orientations homogenises the residual stress distribution. Finally, regarding the checkerboard strategy, the researches point out different results [15].

2.3.4 Reduction of residual stress in AM

If no desired residual stresses are obtained after removing the parts from the plate there are three postprocessing ways of reducing it:

- Baseplate/substrate preheating. This procedure allows to reduce the effect of the temperature gradient mechanism. When the substrate or the building plate is preheated up to a certain temperature the thermal gradient of the part is reduced and therefore less residual stress is induced. The maximum principal residual stress decreases when the bigger the preheating temperature is. This fact has been widely agreed in the literature and simulations also have proved it[15][19].
- Annealing. It is a common heat treatment in metallurgy and it involves heating the material above its recrystallization temperature and holding this temperature for a certain period. Finally, a cooling process is applied. When the part is above its recrystallization temperature, recovery and recrystallization phenomena appear, the strained grains are replaced by grains that start to appear and expand. Usually a fine grain structure is desired and for that reason the recrystallization temperature is hold until that desired grain size is obtained. Cooling process applied is slow in order to avoid big temperature gradients and thus the residual stress appearance. Depending on the part size, the cooling rate is different due to the thermal conduction phenomenon. In additive manufacturing this process has shown a reduction of the residual stresses in the manufactured parts[15][18][19].
- Shot peening or laser peening[19]. It consists in shooting small round metallic or ceramic balls to the part. The balls impact the surface with enough force to create a plastic deformation. This process is used to induce a layer compressive residual stress and modify the mechanical properties of the metals improving its fatigue strength. When the compressive residual stress is induced by a laser this process can be also known as laser peening.

2.4 17-4 PH

17-4 PH (also known as AISI 630, UNS S17400 or DIN 14542 or DIN 14548) is a martensitic precipitation hardened stainless steel. This steel alloy is characterized by having chromium, nickel and copper in its microstructure and also for having a precipitation hardening heat treatment as a postprocess. As a result, this material has high hardness and corrosion resistance which make this material very suitable for aerospace, food processing and chemical industry. According to EN 14542 its chemical composition (%) is presented (Table 2.1):

	Cr	Mn	Si	Ni	P	S	C	Cu	Cb+Ta
Min	15	-	-	3	-	-	-	3	0,15
Max	17,5	1	1	5	0,04	0,03	0,07	3,5	0,45

Table 2.1 Chemical composition of 17-4 PH (%) according to EN 14542

A thermal treatment is always applied to this alloy, as the material name shows this heat treatment is called precipitation hardening (also known as age hardening or particle hardening). This heat treatment is used to increase its strength and hardness and it consists in 3 steps (Fig. 2.8):

- Solution Annealing. (See 2.3.4). The part is maintained at the chosen temperature until there is only one phase. In the case of 17-4 PH, we can find mainly the austenite phase with the rest of the elements of the solution in the element matrix.
- Quenching. Consist in a rapid cooling stage of the annealed solution. The rapid cooling does not allow diffusion of the carbon in the austenite phase creating a metastable phase known as martensite, which is not tempered. The other elements also do not have time to diffuse. Then the solid solution is supersaturated.
- Precipitation (Aging). Just after the quenching process an intermediate reheating step is applied. During this process the martensite is tempered and raises its material ductility while its hardness is lowered. In addition to this, a new phase starts to appear into previously formed martensite in form of small precipitates. These precipitates appear homogeneously in the grains and change the original phase

matrix and prevent the dislocations from moving, which rises the material yield strength and its ultimate strength. As a result, the material is hardened.

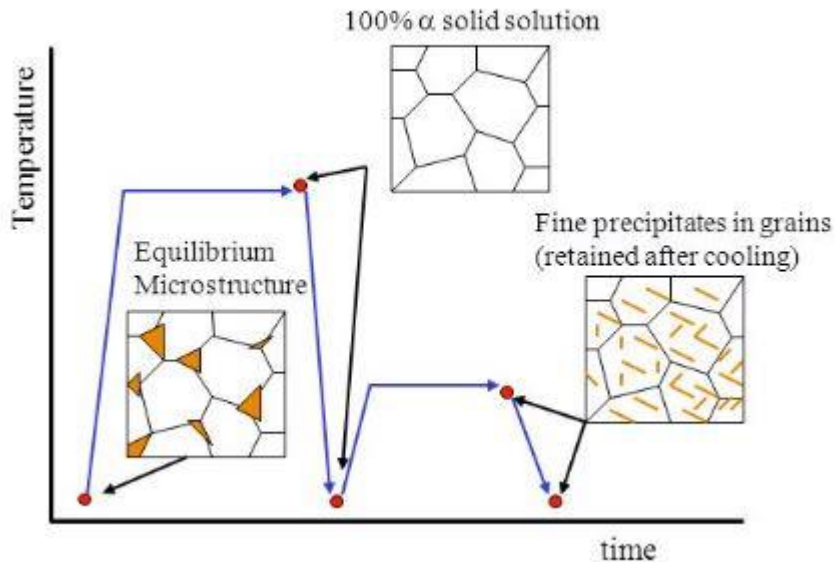


Fig. 2.8: Precipitation hardening process[25]

Regarding its behaviour and the performance of AM parts, some studies were done in that field. As expected, the very high cooling rates result in non-equilibrium phases such as martensite, but also the highest cooling rates lead to another phase known as retained austenite [11], which becomes martensite once strain is applied and then the part hardens (because of the martensite). Nevertheless, this retained austenite inhibits the hardening when applying the precipitation process[26].

All studies agree on the fact that performing the whole heat treatment (Solution annealing + quenching + precipitation) improves its mechanical properties [11][27] and also gives the same microstructure as the wrought material [28]. In addition, residual stresses during the precipitation hardening are also reduced in the annealing process [11][29].

Even though several studies were carried out to study its mechanical properties with different parameters, regarding residual stresses and distortion, there is currently only one study related to residual stresses of 17-4 PH[30]. In this investigation specimens were manufactured and a heat treatment was applied in some of them. Finally, the residual stresses were measured by neutron diffraction method. The results show that residual stresses are reduced in the heat treatment and in some cases, they change from compressive residual stress to tensile residual stress. Regarding the residual stresses distribution central layers show a compressive axial residual stress except some points measured in the surface that got tensile residual stress. The lowest layer shows also tensile residual stress. Comparing this results to what other

authors point out about residual stresses distribution[14][17] we can conclude that, in general, they follow the same residual stress profiles as the one found in other articles. However, the surface shows tensile residual stresses, a discussion about this result should be done in order to contrast it with the models.

2.5 Simulation of AM process

As it has been seen before, there are too many variables in the process and interactions between parameters that makes it difficult to understand. In these cases, the finite element method (FEM) simulation approach can be useful to explore the final properties and the behaviour of the process with different parameters without investing money on experiments. Even though 3D printing is a new process, there are some equations that intend to simulate the whole process and its mechanical behaviour. Depending on the physical considerations and its timescale, 3 types of simulation can be found[31]:

- Microscale simulation. These types of models are based in the heat absorption, the interaction of the material and its phase changes during in a small domain comparable to the size of the layer thickness (between $1 \cdot 10^{-6}$ and $1 \cdot 10^{-2}$ m each element size). These micromodels provide knowledge about the thermal cycle and the different microstructures around the melted and solidified layers.
- Macroscale simulation. These models use the fixed layer size and the thermal cycle applied to calculate the residual stresses and distortion of the part being manufactured. The phase change is not considerate and neither the details of the feedstock. The final properties are calculated based on its thermal cycle and history. These simulations considerate the powder deposition and the clamping conditions as boundary conditions[31]. A further description of the macroscale simulation and modelling is explained in the next section.
- Mesoscale simulation. These simulations try to describe the composition and the mechanical properties of the material. This information is used after with the macroscale and the microscale simulations.

2.5.1 Macroscale simulation

As it has been said before, the macroscale simulation is only based on the thermal cycle applied and its evolution over time. The physics of the heat interaction between feedstock and substrate are not modelled and calculated and neither its heat transfer and phase change. As a first approach the effect of the phase change is it not considered and the heat supplied is mainly transferred to rest of the manufactured part by thermal conductivity. The different thermal situations of the cycle (rapid heating, rapid cooling, thermal conduction, convection of the chamber...) are expected to lead to temperature gradients, then thermal stresses appear and as a result residual stresses are induced. In addition, the cutting stage and unclamping also affect to residual stress. Also, these thermal gradients lead to distortion due to the changes of the thermal expansion of the material because it also changes with temperature. The only residual stresses calculated are the macro-stresses (Type I) due to the scale of the simulation.

This section is intended to explain how Simufact Additive macroscale simulation works[32]. The macroscale simulation of AM approach it is based in a thermomechanical weakly-coupled simulation and it is divided in two parts. The first part consists in the calculation of the temperature field of the built part using the governing equation, the initial boundary equations and the loads applied. To obtain this, the desired part is discretized into voxels that will be the elements during the simulation. Each voxel has several layers and Simufact Additive works with several voxel layers during the building stage. Each building stage is split into several steps and in every step the temperature field is calculated[32].

Once the temperature field is calculated, a mechanical analysis is performed using the temperature field. The interactions between temperature and stress fields are not calculated. If the interactions between temperature fields and stress are taken into account then it requires more calculation time. Simufact Additive does not always perform the thermomechanical weakly coupling in every building step of each voxel layer, instead of this it performs the thermomechanical weakly coupling at defined time steps in each voxel layer during its building process[32].

In the SLM process the temperature field can be found by solving the heat conduction equation according to Fourier's law Eq.(3)[31][33]:

$$\frac{\partial(\rho(T)h(T))}{\partial t} = \nabla \cdot (k(T)\nabla T(x, y, z, t)) + Q(x, y, z, t) \quad (3)$$

Where ρ is the density, h is the specific enthalpy of the material, k is the thermal conductivity and Q is the net volumetric source applied that comes from the laser action. Then, regarding

this equation, the thermal analysis becomes non-linear because of the temperature dependent material properties and transient due to its evolution over the time. The net volumetric source applied can be defined using energy density Eq.(1) and scanning rate Eq.(2) as the following Eq.(4):

$$Q(x, y, z) = \eta E = \frac{\eta P}{\dot{V}} \quad (4)$$

Where η is the efficiency factor of the laser, it accounts for all energy lost prior the beam heats the power during the adsorption and P is the laser Power. The enthalpy can be calculated using:

$$h(T) = \int c_p(T) dT \quad (5)$$

Where c_p is the heat specific capacity.

In Simufact Additive, once the metal powder becomes liquid the material properties of the bulk material are applied and the stresses and strains are set to zero. Regarding the material properties conditions, the thermal expansion coefficient is set to zero, the yield stress is scaled up to avoid plastic deformation and the materials properties are scaled with a mechanical scaling factor. Finally, when the material becomes solid the stresses and strains are calculated and the material data from bulk material is considered without scaling factors[32].

The boundary conditions are set considering that the first powder layer has the temperature of the building plate. When a new layer is built, there is a heat flux going from the layer to the building chamber. For every element of the solid border, a heat flux normal to the surface due to thermal conduction has to be equal to the heat flow of convection and radiation. The boundary condition equation of the building plate Eq.(6) and the boundary condition of heat flux at the border Eq.(7) are:

$$T(x, y, 0, 0) = T_{plate} \quad (6)$$

$$-k(T)\nabla T(x, y, z, t) = h_c(T(x, y, z, t) - T_\infty) + \epsilon\sigma_{sb}(T(x, y, z, t)^4 - T_\infty^4), \quad (7)$$

$$\forall x, y, z, t \in \partial\Omega_s$$

T_{plate} is the temperature of the building plate, h_c is the heat transfer coefficient, ϵ is the emissivity of the material and σ_{sb} is the Stephan Boltzmann constant. Eq.(7) is applied to every element belonging to the border of the manufactured part ($\partial\Omega_s$).

After applying these equations, the temperature field can be calculated. Once the temperature field is calculated the mechanical analysis is coupled. First of all, the total strain \mathcal{E} (distortion) is split into two components Eq.(8):

$$\mathcal{E} = \mathcal{E}_e + \mathcal{E}_*, \quad (8)$$

Where \mathcal{E}_e is the elastic strain and \mathcal{E}_* is called the inherent strain. The elastic strain \mathcal{E}_e can be modelled using Hooke's Law according to the following Eq.(9)[31]:

$$\sigma = \mathcal{C} \mathcal{E}_e \quad (9)$$

Where \mathcal{C} is the material stiffness tensor and σ is the stress tensor Eq.(10):

$$\mathcal{C} = \frac{E}{(1+\nu)(1-2\nu)} \begin{pmatrix} 1-\nu & \nu & \nu & 0 & 0 & 0 \\ \nu & 1-\nu & \nu & 0 & 0 & 0 \\ \nu & \nu & 1-\nu & 0 & 0 & 0 \\ 0 & 0 & 0 & 1-2\nu & 0 & 0 \\ 0 & 0 & 0 & 0 & 1-2\nu & 0 \\ 0 & 0 & 0 & 0 & 0 & 1-2\nu \end{pmatrix} \quad (10)$$

Where E is the Young Modulus and ν is Poisson's Ratio. Both parameters are temperature dependent mechanical properties. Simufact Additive avoid using a Poisson's Ratio temperature dependent because it has been proven that it has a minimum influence[32]. The values of Young Modulus are very low near melting temperature and Simufact recommends to not to use values smaller than 5GPa because the simulation would be very unstable. If a small deformation is considered, the stiffness tensor multiplied by the total deformation gives the total stress. This fact is also used in different in simulation models in the literature[15].

The inherent strains are highly dependent to the material properties and Simufact Additive offers the chance to simulate using constant inherent strains. The simulation using constant

inherent strains is faster than the ones with no constant parameters. Nevertheless, the constant inherent strains have some disadvantages: the constant inherent strains are calculated using 3D printed real cantilevers and they can only be used with simulations with the same manufacturing parameters. In case of using different process parameters a new cantilever test must be performed. Hence, inherent strains simulations are only used when the manufacturing parameters are always fixed.

In the case of not using constant inherent strains. The inherent strains can be split into three terms calculated with the following Eq.(11):

$$\varepsilon_* = \varepsilon_p + \varepsilon_{th} + \varepsilon_{ph}, \quad \varepsilon_{ph} = 0 \quad (11)$$

Where ε_p is the plastic strain that can be calculated using flow curves with a different range of temperatures, ε_{th} is the thermal strain due to the temperature changes. ε_{ph} is the strain caused by the phase change and can be neglected because his influence is considered not as big as the other strains of the equation. In this case big deformations are considered due to plastic deformation. The thermal strain is calculated using Eq.(12)[34]:

$$\varepsilon_{thermal} = \alpha(T)\Delta T, \quad (12)$$

Where α is the volumetric expansion factor. This parameter is highly sensitive in the simulation according to Simufact Additive[32].

Now the stress distribution is found by solving the mechanical equations with the equations of equilibrium. According to the definition of residual stress, if there are no body forces applied. the equilibrium equation is described as the following Eq.(13):

$$\nabla \cdot \sigma + \vec{b} = 0 \quad (13)$$

Where \vec{b} is body force vector, which a vector that characterises the internal forces between particles of the continuum field. In this case the only internal forces considered are the forces due to gravity. If gravity effect is not considered then \vec{b} can be neglected.

The displacements are obtained by the strain definition Eq.(14) and Eq.(15)[34]:

$$\varepsilon_x = \frac{\partial u}{\partial x}, \varepsilon_y = \frac{\partial v}{\partial y}, \varepsilon_z = \frac{\partial w}{\partial z} \quad (14)$$

$$\varepsilon_{xy} = \frac{1}{2} \left(\frac{\partial v}{\partial x} + \frac{\partial u}{\partial y} \right), \varepsilon_{xz} = \frac{1}{2} \left(\frac{\partial w}{\partial x} + \frac{\partial u}{\partial z} \right), \varepsilon_{yz} = \frac{1}{2} \left(\frac{\partial w}{\partial y} + \frac{\partial v}{\partial z} \right) \quad (15)$$

Where u, v and w are the x, y and z displacements. The boundary conditions for the displacements of the first layer at the beginning of the simulation are 0 Eq.

(16)[34]:

$$u(x, y, z, 0) = 0, v(x, y, z, 0) = 0, w(x, y, z, 0) = 0, \forall z \in 1st \text{ layer} \quad (16)$$

3 Methodology

With the aim of performing the sensitivity study, the simulation software Simufact Additive was used in this project. The type of simulation used was a thermomechanical macroscale simulation, which takes a lot of time depending of the voxel size: small voxel size means more elements and therefore more precision but also more calculation time. Because of this, a single part voxel mesh study was decided to be performed. Nevertheless, the sensitivity study was chosen to be performed with more than one part because 3D printing companies print many parts at the same time to save money and production time.

Specimens used in the simulation were printed in the same machine at the same time. A post-process heat treatment (precipitation hardening) was also applied to the specimens. The specimens design was carried out by the Mechanical Engineering department and its shape was chosen in order to perform other tests in other projects of the same department (Fig. 3.1). The axial Residual stresses were measured in three points of the surface of each specimen centre via X-Ray diffraction. In total two specimens were measured. The residual stresses results were compared to the single specimen simulation and the sensitivity study simulations. No distortions were measured.

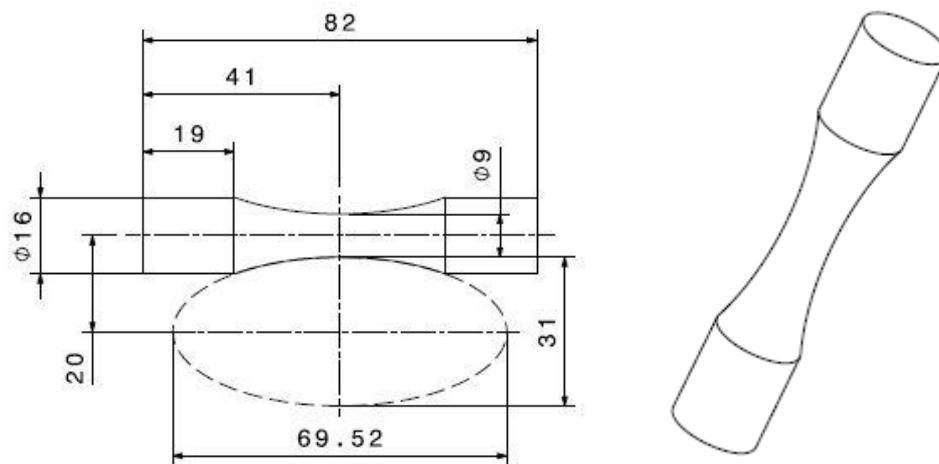


Fig. 3.1: Specimen design

4 Residual stress measurements

Two specimens after precipitation hardening were measured via X-Ray diffraction. Three times each specimen was measured in its centre section (41mm height). Each measurement point chosen was on the surface and all of them formed 120° between the other points. The following table (Table 4.1) shows the Z residual normal stress results:

	Residual σ_z [Mpa]	
	Specimen 1	Specimen 2
1	0±26	0±19
2	30±21	0±16
3	0±29	32±21

Table 4.1: Residual σ_z results of the measurements

As we can see all the values measured have the mean greater or equal than zero. However, its uncertainty (denoted by \pm) can lead in some measured points to compressive residual stresses but mostly its values are positive and hence tensile. Moreover, in 4 out of 6 measurements the mean of stresses were 0. To conclude the testing phase, it can be said that the specimens with heat treatment applied lead to almost no residual stresses. However no previously data before applying the heat treatment was obtained and we cannot estimate the reduction of residual stresses due to heat treatment.

5 Single Specimen

5.1 Procedure

A voxel mesh study was carried out with the default parameters of Simufact Additive. The voxel mesh size was changed from 0,5 mm to 2mm in 0,25 mm size increments. Normal Z Residual stresses (Residual σ_z) and distortions were measured in the perimeter of the center section of the specimen (41mm height), each node of the voxels that belonged to that section was measured. Finally, the average of residual stresses and distortions was calculated.

Regarding the parameters of the simulation, the parameters were given in a range of values. Some of the values were not modified and it was decided to use the default values of Simufact Additive and the heat treatment cooling rates were chosen based on the literature. The main simulation parameters chosen for the single specimen simulation were the following:

- Machine: EOS M290
- Laser power: 200 W
- Efficiency: 80%
- Speed: 600 mm/s
- Layer thickness: 0,02 mm
- Beam width: 0,05mm
- Recoater time: 5 s
- Base plate: 30mm
- Heat treatment conditions:
 - Solution annealing at 1050 °C for 30 min. Chosen heating and cooling rate of 10°C/s.
 - Age hardening at 600°C for 4 hours. Chosen heating and cooling rate of 2°C/s.

It was seen that the heat treatment simulation could not be performed because material data was lacking. To solve this issue, new material data regarding creep law and flow curve was found in the literature and was added to the data library. In addition, more data related to mechanical properties of 17-4 PH were also found and added. The discussion and the values of the new material data was discussed in section 5.1.1 . The new material data was added incrementally to the library and simulations (these simulations were performed also with 1mm voxel mesh size); the effect of the different new material data in the residual stress and the distortion is also showed in results. Finally, the comparison with the single heat-treated simulated specimen and the printed ones has been done.

5.1.1 New material added

The default material library of 17-4 PH powder did not allowed to perform heat treatment conditions because it was lacking of data. Considering that other materials of the library use properties of the bulk material, it was decided to complement the default library of 17-4 PH. Searching in the literature allowed to add a new data regarding creep law and flow curves [35]. The paper used investigated and calculated the hot working characteristics and creep laws of 17-4 PH. Compressive tests experimental data was gathered at different temperatures and strain rates. Even though $0,001 \text{ s}^{-1}$ strain rate flow curves were added (Fig. 5.1), more flow curves could have been added. This is because in Simufact Additive every strain rate must have all the flow curves for every temperature and the default temperatures in the library were only at $0,001 \text{ s}^{-1}$ strain rate. A hyperbolic creep law was found with a coefficient of determination of 0.96 and was added to the library Eq.(17).

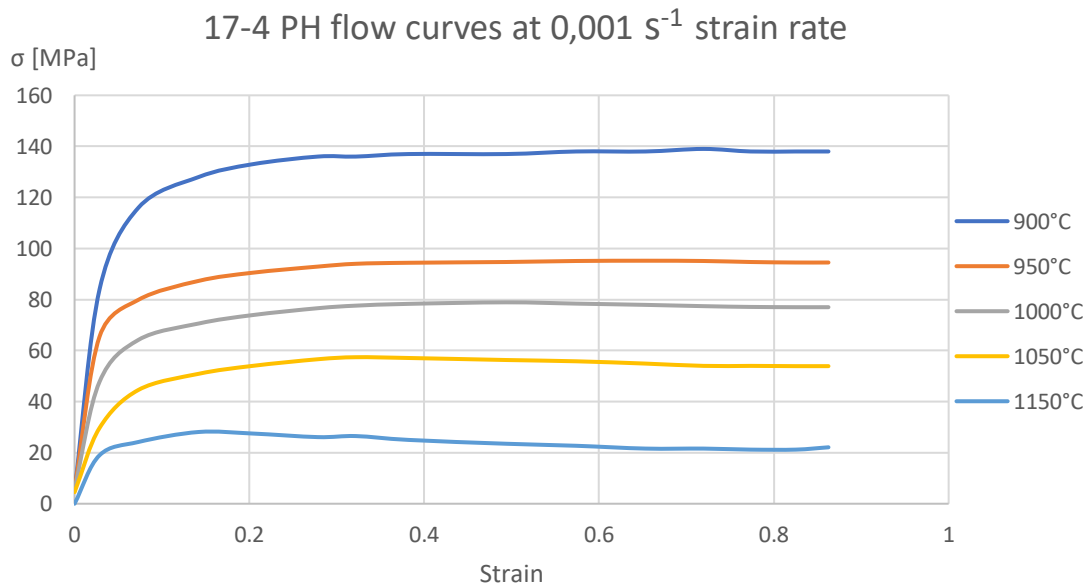


Fig. 5.1: New flow curves at $0,001 \text{ s}^{-1}$ strain rate added

$$\dot{\epsilon} e^{460 \cdot 10^3 / RT} = 1,053 \cdot 10^{16} \cdot (\sinh(0,0105 \cdot \sigma))^{4.828} \quad (17)$$

Comparing 17-4 PH library with other materials library (e.g Ti-Al6-4V), there were many differences regarding thermal and mechanical information added. Whereas others materials have table data properties, 17-4 PH has only constants. The table data allows to interpolate values and therefore to get more accurate results. Thermal conductivity and Young's Modulus data were found in the literature[36]. In the investigation 17-4 PH casting data was compared to wrought material. Both materials show same tendency and similar values of thermal

conductivity and Young's modulus. Moreover, the default data fits into this table data. The casting data was decided to be used in the simulation rather than the wrought material because it fits better in the AM process due to melting and heating process. The following data added is presented and compared to the default data (Fig. 5.2)(Fig. 5.3):

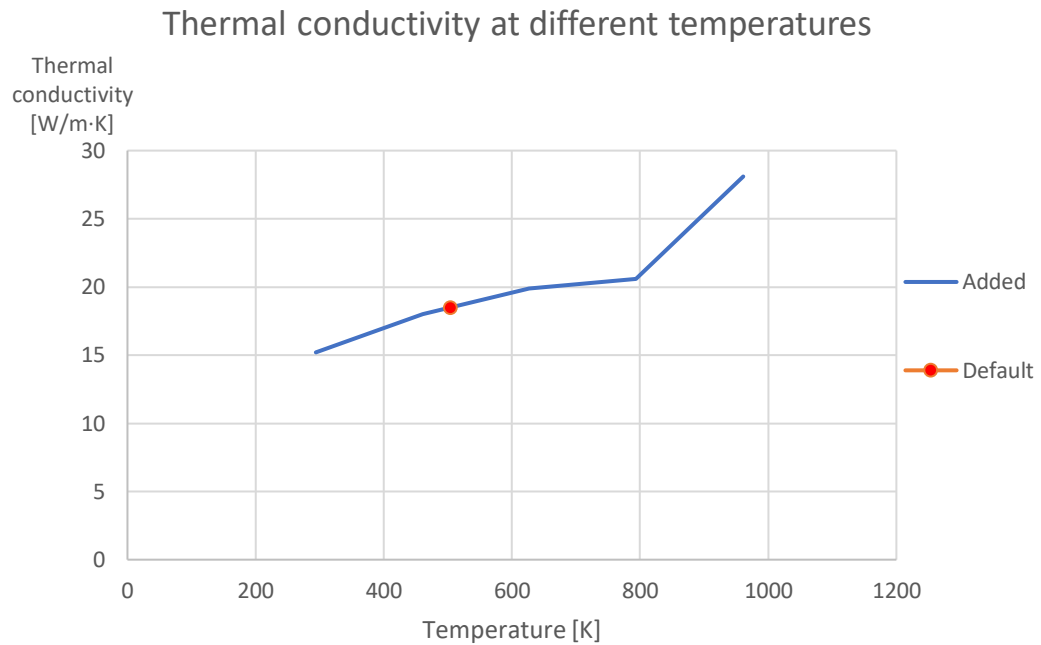


Fig. 5.2: Thermal conductivity at different temperatures: data added vs default

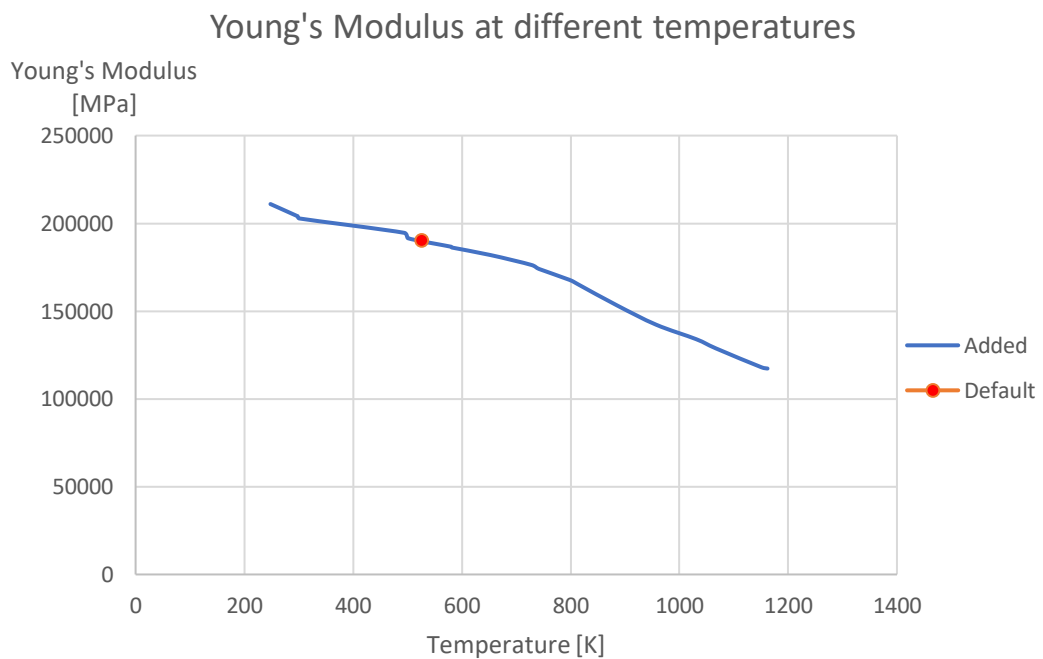


Fig. 5.3: Young's Modulus at different temperatures: data added vs default

Comparing the thermal expansion coefficient, there is also the same problem regarding table data, there was only one constant in the default library of 17-4 PH. Simufact Additive also remarks that thermal expansion coefficient is highly sensitive[32]. Data regarding thermal expansion of 17-4 PH was found in the literature[37]. The paper mentions that it is the martensite transformation in the cooling process that induces residual compressive stresses. However it is also pointed out that the different cooling rates can change the different values of the thermal expansion coefficient [37]. Finally the default data has the value compressed into the interval of the new data and it was decided to be added to the material library (Fig. 5.4):

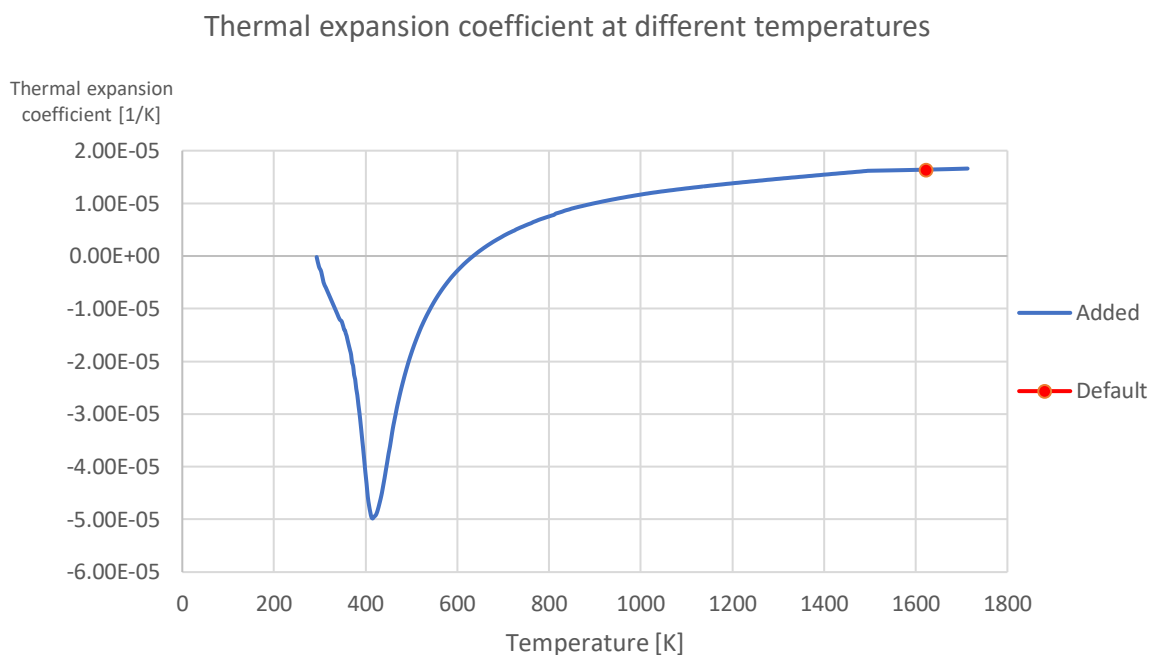


Fig. 5.4: Thermal expansion coefficient at different temperatures: data added vs default

5.2 Results

5.2.1 Voxel mesh study

The results of the voxel mesh study are presented in this section (Fig. 5.5)(Fig. 5.6):

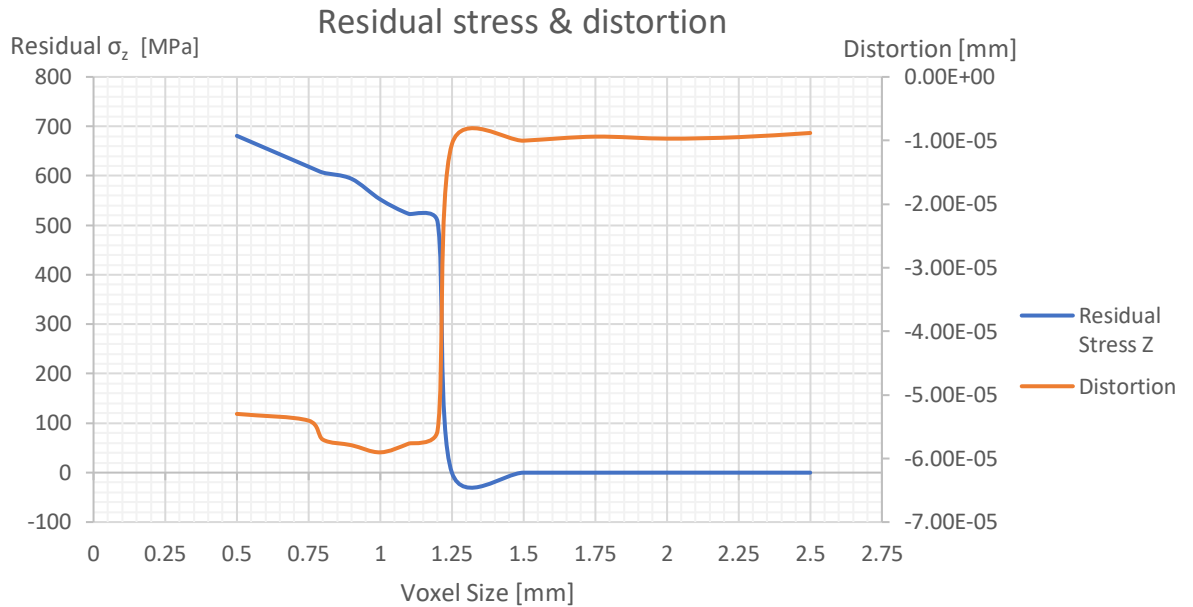


Fig. 5.5: Residual stress and distortion at different voxel sizes

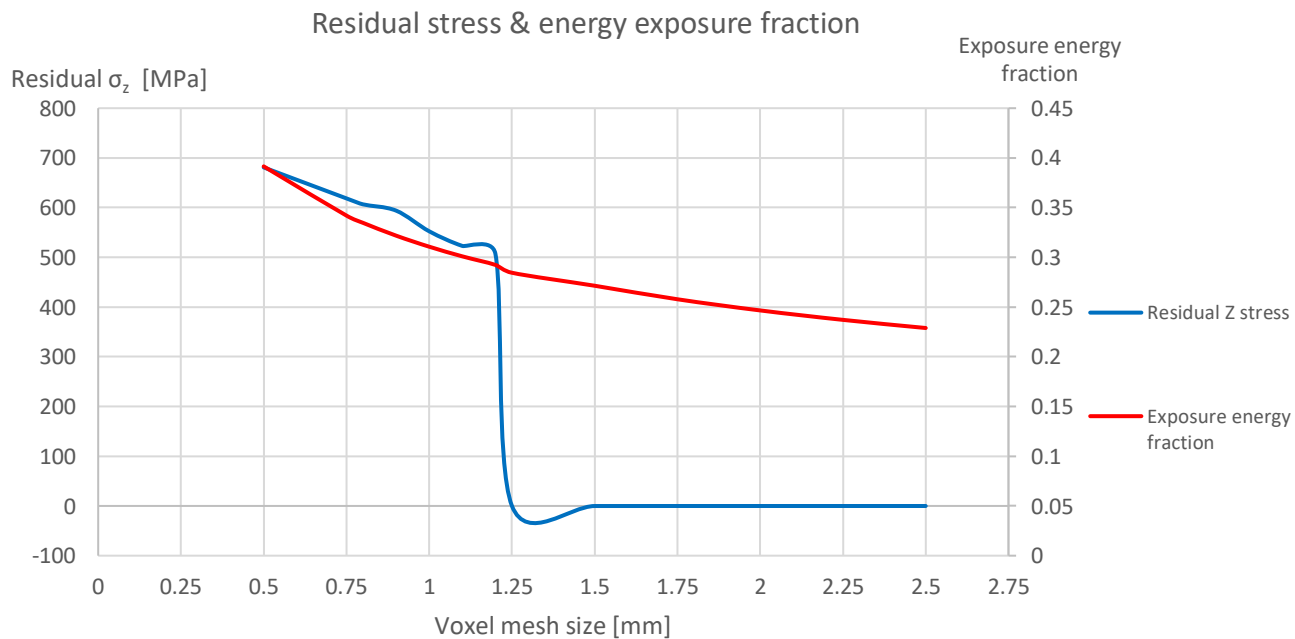


Fig. 5.6: Residual stress and exposure energy fraction at different voxel sizes

We can see that residual stresses and distortions change abruptly in the band between 1mm and 1.5mm voxel mesh size. A relation between this change and energy exposure factor has been showed, the higher the value of energy exposure factor, the higher the residual stresses and the lower the distortions, the distortions tend to zero specially at high voxel sizes.

5.2.2 Default data vs new data

5.2.2.1 Residual stress

The following pictures show the residual stress in the simulation with 1mm voxel size with the default material data (Fig. 5.7), the new material data added (Fig. 5.8) and the new material data with the heat treatment added (Fig. 5.9). Furthermore, the evolution of the new material data is also showed: a boxplot with the residual stress values of the nodes in the section where the real specimens were measured is presented (Fig. 5.10) and also the evolution of its residual stress average (Fig. 5.11):

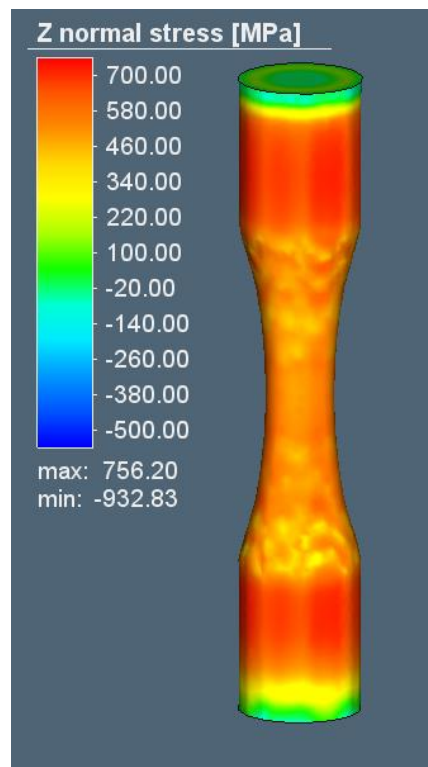


Fig. 5.7 Single specimen residual σ_z with data by default

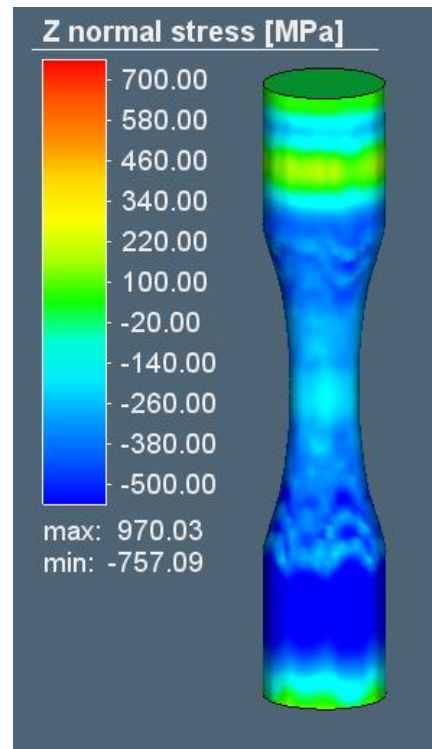


Fig. 5.8: Single specimen residual σ_z with new data added without heat treatment

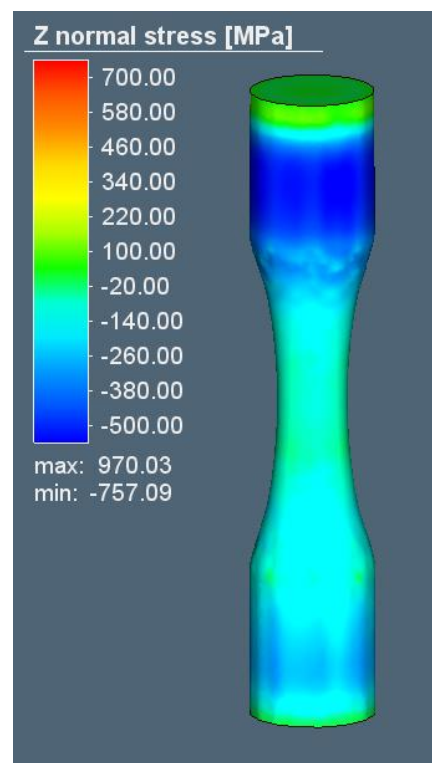


Fig. 5.9: Single specimen residual σ_z with new data added and heat treatment

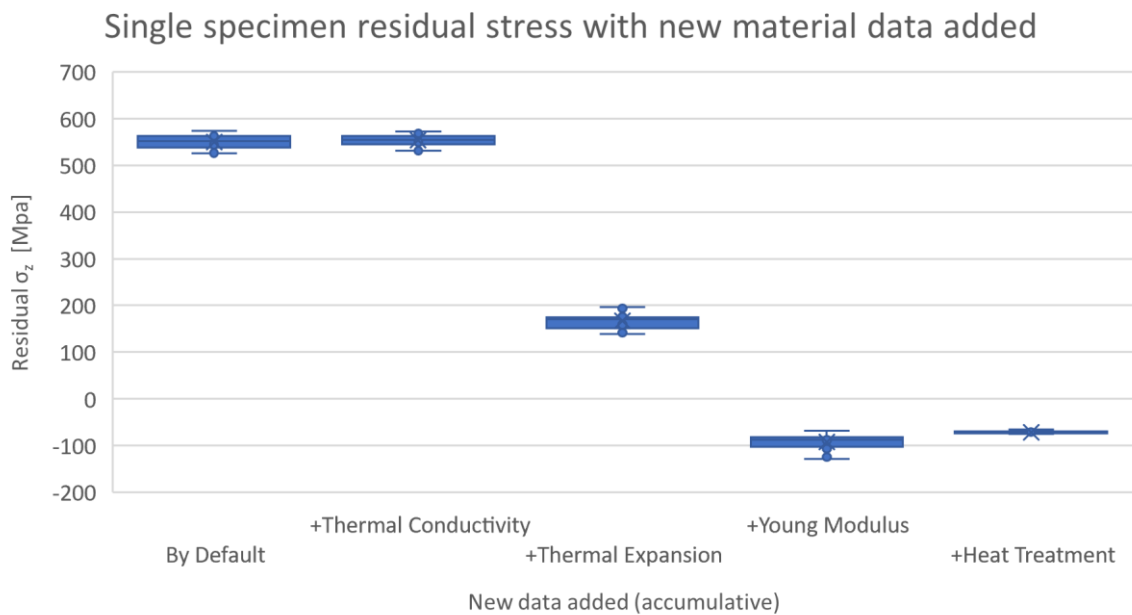


Fig. 5.10: Boxplot single specimen residual σ_z with new material data added accumulatively in the measured section

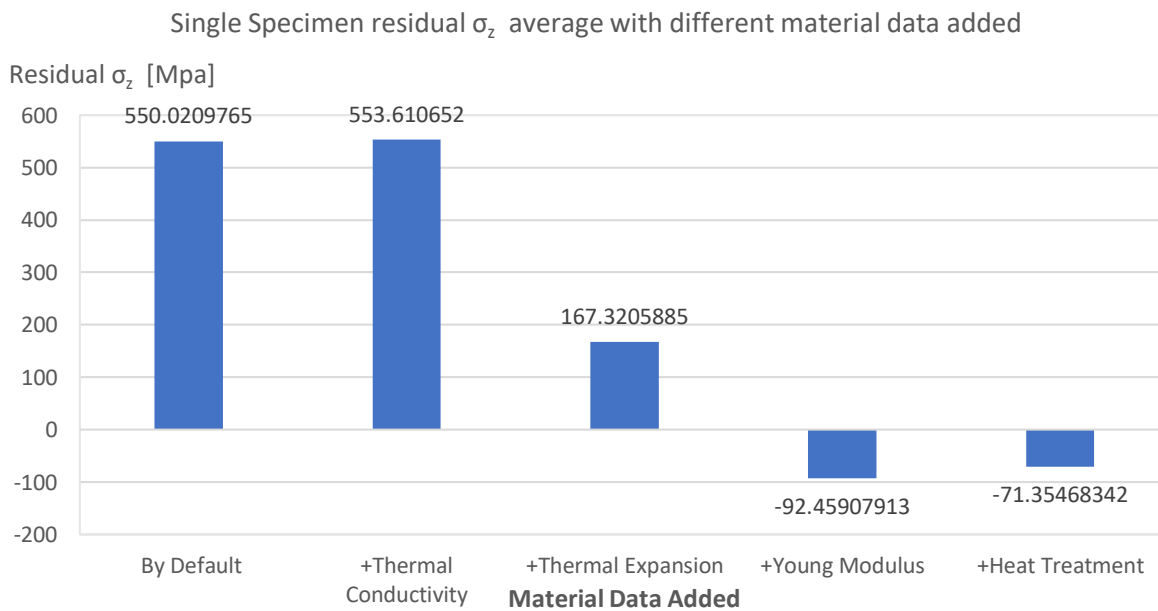


Fig. 5.11: Single specimen residual σ_z average with new material data added accumulatively in the measured section

By adding the new material data, residual stresses in all the part are reduced except when the thermal conductivity was added, the heat treatment shows a reduction of the residual stresses on average in a 22%. The residual stresses in the measured area with the default material were tensile while with the new data added and the heat treatment were found to be compressive. The change from tensile residual stress starts when the Young modulus is

added. A big difference between material data added and data by default is observed. However, a pattern is observed in the top layer and the lowest layer, both are the ones that have residual stress tensile. Finally, the thermal treatment showed a reduction in the compressive residual stresses.

5.2.2.2 Distortion

The following pictures show distortion in the simulation with 1mm voxel size with the default material data (Fig. 5.12), the new material data added (Fig. 5.13) and the new material data with the heat treatment added (Fig. 5.14). Also, the evolution of maximum and minimum distortion with the data added is also showed (Fig. 5.15):

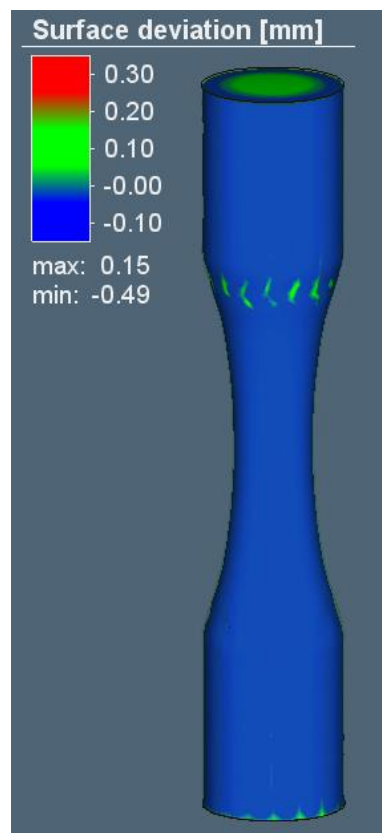


Fig. 5.12: Single specimen distortion with data by default

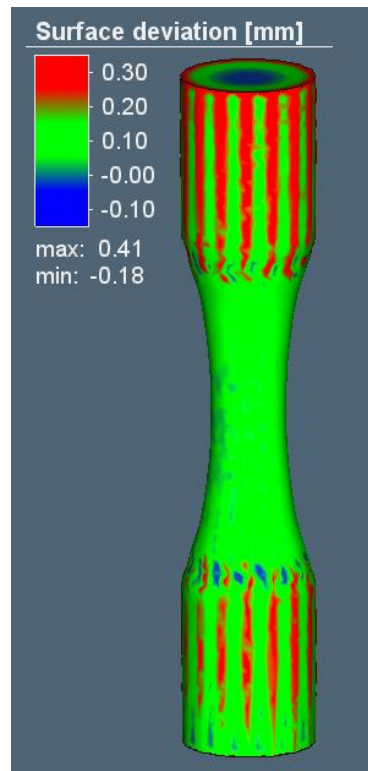


Fig. 5.13: Single specimen distortion with new material data added without heat treatment

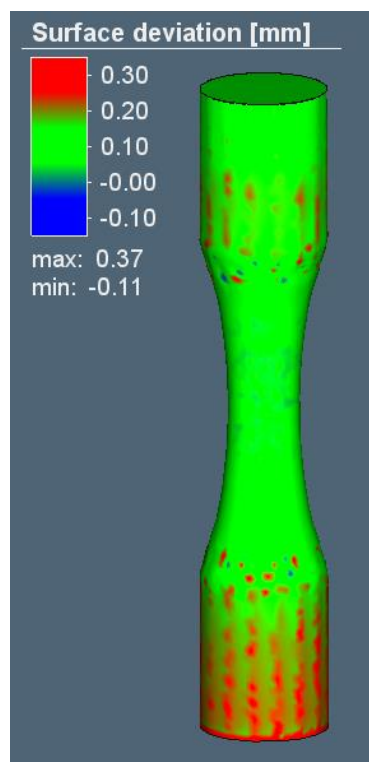


Fig. 5.14: Single specimen distortion with new material data with heat treatment

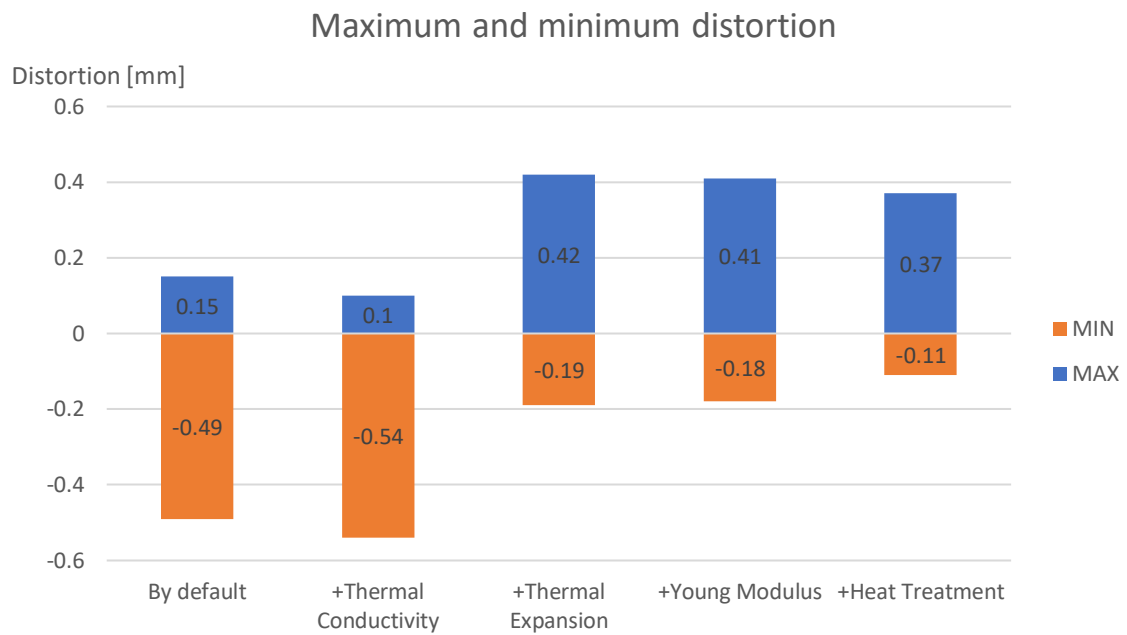


Fig. 5.15: Single specimen maximum and minimum distortion with new material data added

With the new material data added the distortions change drastically. Whereas with the material default data the distortions are negative, with the new data added and the heat treatment the distortions are positive. This change can also be seen with the maximum and minimum distortion. The big change starts when the thermal expansion is added. Before adding the thermal expansion, the minimum distortion was bigger than the maximum and after adding the thermal expansion the maximum distortion became bigger than the minimum. Heat treatment reduced the maximum and the minimum distortion. A big difference is observed between the material added and the default data.

5.3 Discussion

The results of the mesh study related to residual stress and distortion change drastically with different voxel sizes. This fact can be attributed to the energy exposure fraction that depends on the voxel size. It is not possible to find an optimal voxel mesh size due to the lack of convergence values and the drastic change in the band between 1,5 mm and 1mm. The energy exposure fraction requires to be calibrated via Thermal simulation and it also requires data from a real test. No value output can be obtained from the voxel mesh size study but we can see that the distortion vs residual stress follows the rule of welding (Fig. 2.4).

The new material data added versus the default data showed a different profile. Whereas in the simulation run with default data the Z normal residual stress distribution have the middle region more tensile and the top layer and the bottom layer are less tensile, the simulation run

with the new data showed that in the middle region the Z normal residual stress distribution is compressive and the top and bottom zone are tensile. With the new material data, the residual stress distribution is equal to what other scientific research have found[18] [23]. Moreover, we can observe also a pattern between residual stresses and distortion. When the residual stresses are tensile, the distortions are compressive and vice versa. This phenomenon also occurs with the maximum and minimum residual stresses and distortions. We can say that a similar pattern to the welding rule is obtained.

By adding new data progressively, the residual stress in general changes from tensile to compressive. The big changes occur when the thermal expansion and the young modulus are added. The thermal expansion changes the distortion interval drastically as expected due to the curve presents a negative expansion factor (Fig. 5.4), the negative thermal gradient originates expansion when cooling following the Eq(12) . Based on the research about the thermal expansion coefficient[37], the residual stresses should be compressive due to this effect. However, this only happens when the Young Modulus is added. This fact can be explained because the Young Modulus becomes higher when it is cooled and it is combined with thermal expansion, which is lower in most of the temperature range. The highest tensile stress was found when the thermal conductivity was added because the new thermal conductivity data is higher than the default data (Fig. 5.2). When the thermal conductivity is higher, the higher are the thermal gradients induced and then the distortions are higher and thus the residual stresses.

Finally, the heat treatment showed a reduction of residual stresses of the material but the values does not belong to the real specimens measured. This might be because there is only one specimen manufactured and the heat flow is higher than if we manufactured more specimens at the same time or maybe due to the cooling rate applied in the heat treatment that it should be lower in order to reduce the thermal gradient. Another reason could be that this simulation uses the energy density as input value for every voxel layer and it has been seen in the literature that this parameter is not the real energy input[10][12][15][21].

Based on the results obtained we can conclude that the new data added can lead to more realistic results due to its final values that are closer to reality and follow a pattern of residual stresses aligned with the results of previous scientific research. Moreover, the heat treatment showed a reduction of residual stresses. The voxel mesh study was not useful because of the existence of internal parameters that need to be calibrated based on reality. As a result, the next simulations will be done using 1mm voxel mesh based on default values of the software.

6 Sensitivity study

6.1 Procedure

A layout to distribute the specimens in the base plate was. In total 10 specimens were manufactured at the same time at the machine. It was decided to simulate 10 because if more specimens were manufactured the simulation would have lasted longer. Nevertheless, as said before AM companies produce more parts in the same machine at the same time. Regarding the distribution of the specimens in the base plate, they were distributed in 3 rows, the central row had 4 specimens and the other ones 3. Each row had an angle of 45° to the sides of the building plate. The distance between rows was 25 mm and the distance between specimens of the same row was 22 mm (Fig. 6.1):

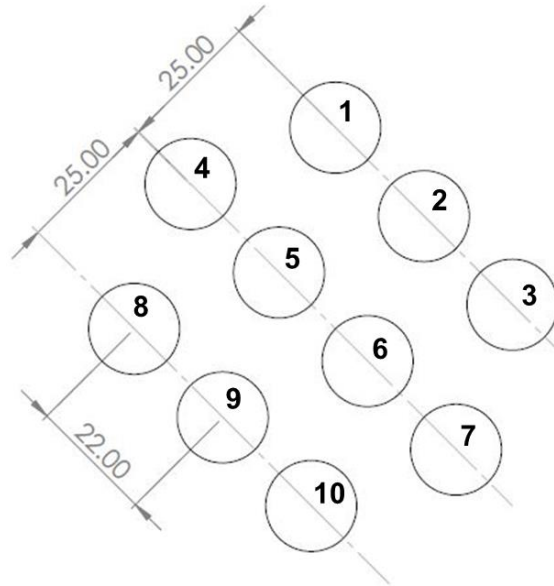


Fig. 6.1: Specimen building layout with numbering and dimensions

Previously to the sensitivity study, a multiple specimen simulation was decided to be performed with all the new material data added and without the new material data to compare. Simulations including heat treatment were also performed. The heat treatment conditions were the same as the single specimen simulations. The voxel mesh size was fixed at 1mm size based on the default value of Simufact Additive software.

The parameters used for the sensitivity study were the efficiency, the beam width and the scanning speed. It was decided to perform the sensitivity study with these parameters because Simufact Additive uses some internal variables that are calculated based on internal parameters, specially exposure energy fraction[32], which it has been seen that affects

distortion and residual stresses in the voxel mesh study. Efficiency, scanning speed and beam width parameters change the energy density and the scan rate, which are parameters widely known. The other parameters used were the same as the single specimen simulation. The levels for the sensitivity study were the following:

- Efficiency (three levels): 80 ,90 and 100%.
- Scan Speed (three levels): 600, 700 and 800 mm/s.
- Beam Width: 0,1 and 0,05 mm.

Normal Z Residual stresses were measured in the perimeter of the centre section of the specimen (41mm height), each node of the voxels that belonged to that section was measured and the average residual stress of each specimen was calculated. Moreover, a distribution of residual stresses in every specimen of the simulation can be found in results. However, in order to get easy data to analyse, every simulation had a Z normal residual stress average that comes from calculating the residual stress average of every specimen. This data was introduced to Minitab and was analysed with a regression model in order to get further information. Moreover, the effect of energy density and scan rate in residual stress was analysed because every simulation had different values of it. Finally, a correlation test was performed with Minitab to relate residual stresses with scan rate and energy density.

Distortions were also calculated but this time in every specimen the maximum and the minimum values were stored. In every simulation the average maximum distortion and the minimum were calculated. Finally, this data was also analysed with a regression model in Minitab to get further information and a correlation test was performed with Minitab to relate distortion with energy density and scan rate.

6.1 Results

6.1.1 Residual Stresses

The next three pictures show the differences between the layout simulation with default material data (Fig. 6.2), with new material data added without heat treatment (Fig. 6.3) and with heat treatment (Fig. 6.4):

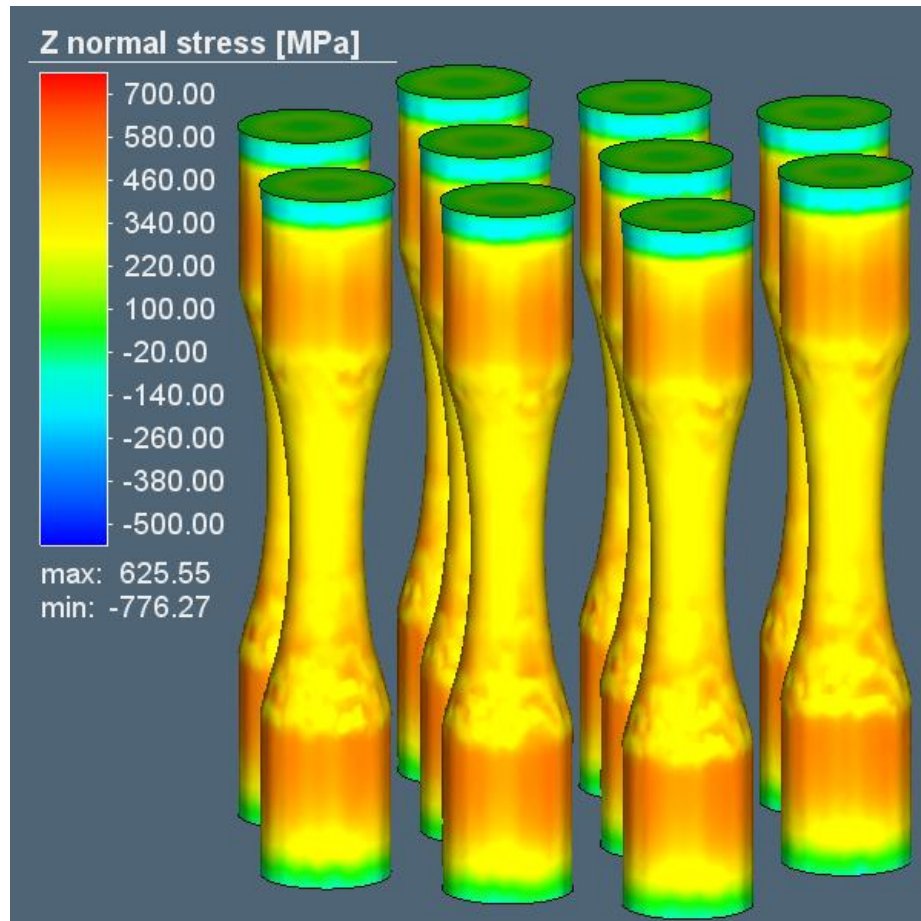


Fig. 6.2: Residual stress simulation with default material data

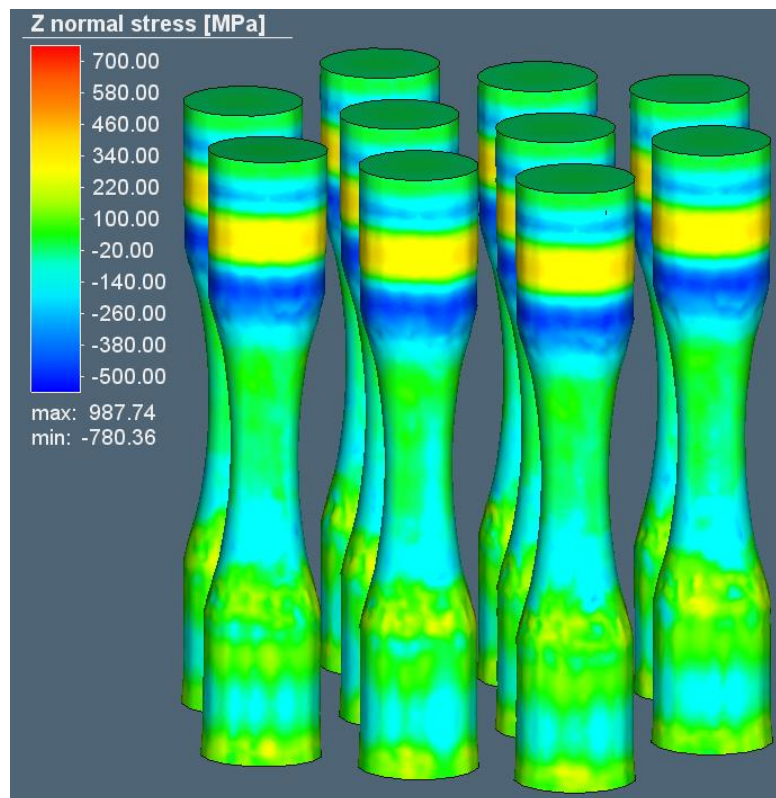


Fig. 6.3: Residual stress simulation with new material data without heat treatment

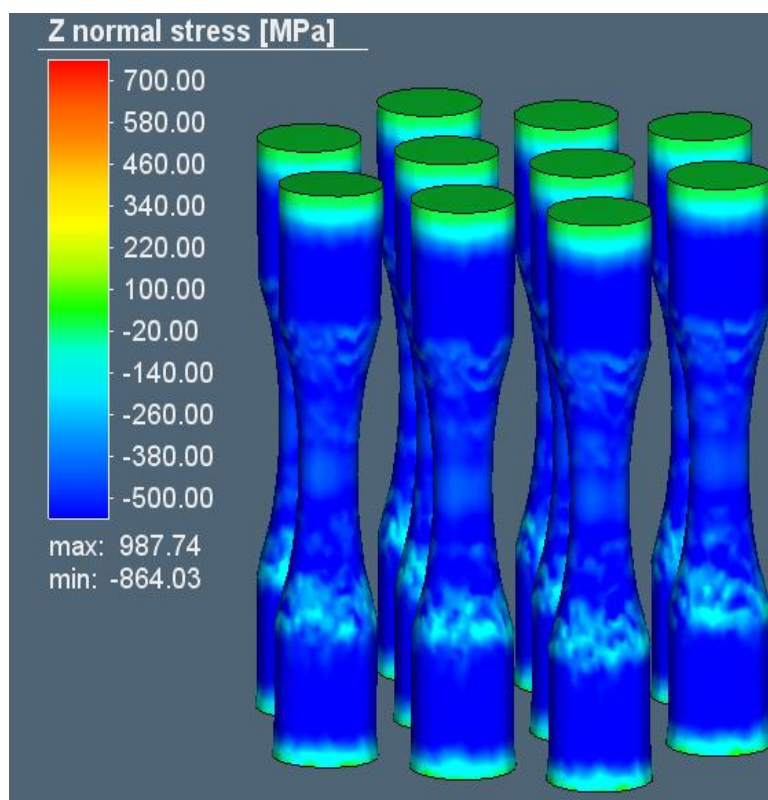


Fig. 6.4: Residual stress simulation with new material data and heat treatment

By adding the new material data, the Z normal stress changes drastically, from being tensile stress to compressive stress in the zone measured. Top part and base part also change, but in that case, they are all both tensile and closer to 0 MPa than other zones of the specimen. The effect of the heat treatment it induced more compressive residual stresses to the parts.

The next table (Table 6.1) shows the average residual stress measured in all the sensitivity study simulations. In addition, energy density and scan rate parameter values are also showed. Each simulation has a different name classified according to efficiency (E), scan speed (S) and beam width (B). In the following pages the distribution of stresses in the measured section is also showed in boxplot diagrams(Fig. 6.5.-Fig. 6.22) Each specimen has a number according to Fig. 6.1.:

Name	Variables			Internal parameters		Results
	Efficiency [%]	Scan speed [mm/s]	Beam width [μm]	Energy density [J/m^3]	Scan rate [m^3/s]	Average residual stress [MPa]
E8-S6-B5	0,8	600	50	3,8E+11	4,2E-10	-34,095
E9-S6-B5	0,9	600	50	4,29682E+11	4,2E-10	-36,370
E1-S6-B5	1	600	50	4,7619E+11	4,2E-10	-41,065
E8-S7-B5	0,8	700	50	3,26531E+11	4,9E-10	-48,434
E9-S7-B5	0,9	700	50	3,67347E+11	4,9E-10	-61,249
E1-S7-B5	1	700	50	4,08163E+11	4,9E-10	-64,488
E8-S8-B5	0,8	800	50	2,85714E+11	5,6E-10	-72,839
E9-S8-B5	0,9	800	50	3,21429E+11	5,6E-10	-63,856
E1-S8-B5	1	800	50	3,57143E+11	5,6E-10	-190,296
E8-S6-B1	0,8	600	100	1,90476E+11	8,4E-10	-119,809
E9-S6-B1	0,9	600	100	2,14286E+11	8,4E-10	-167,187
E1-S6-B1	1	600	100	2,38095E+11	8,4E-10	-152,755
E8-S7-B1	0,8	700	100	1,63265E+11	9,8E-10	-177,664
E9-S7-B1	0,9	700	100	1,83673E+11	9,8E-10	-152,222
E1-S7-B1	1	700	100	2,04082E+11	9,8E-10	-198,200
E8-S8-B1	0,8	800	100	1,42857E+11	1,12E-09	-59,674
E9-S8-B1	0,9	800	100	1,60714E+11	1,12E-09	-203,574
E1-S8-B1	1	800	100	1,78571E+11	1,12E-09	-182,802

Table 6.1: Residual stress sensitivity study results table

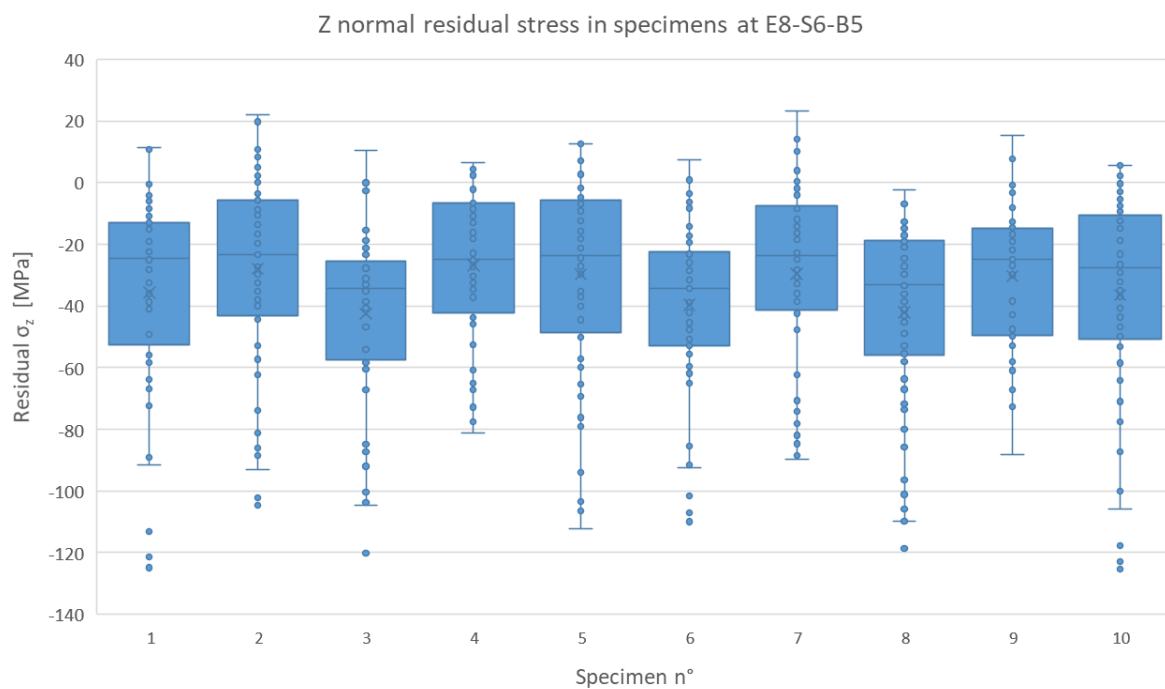


Fig. 6.5: Boxplot of residual σ_z at E8-S6-B5

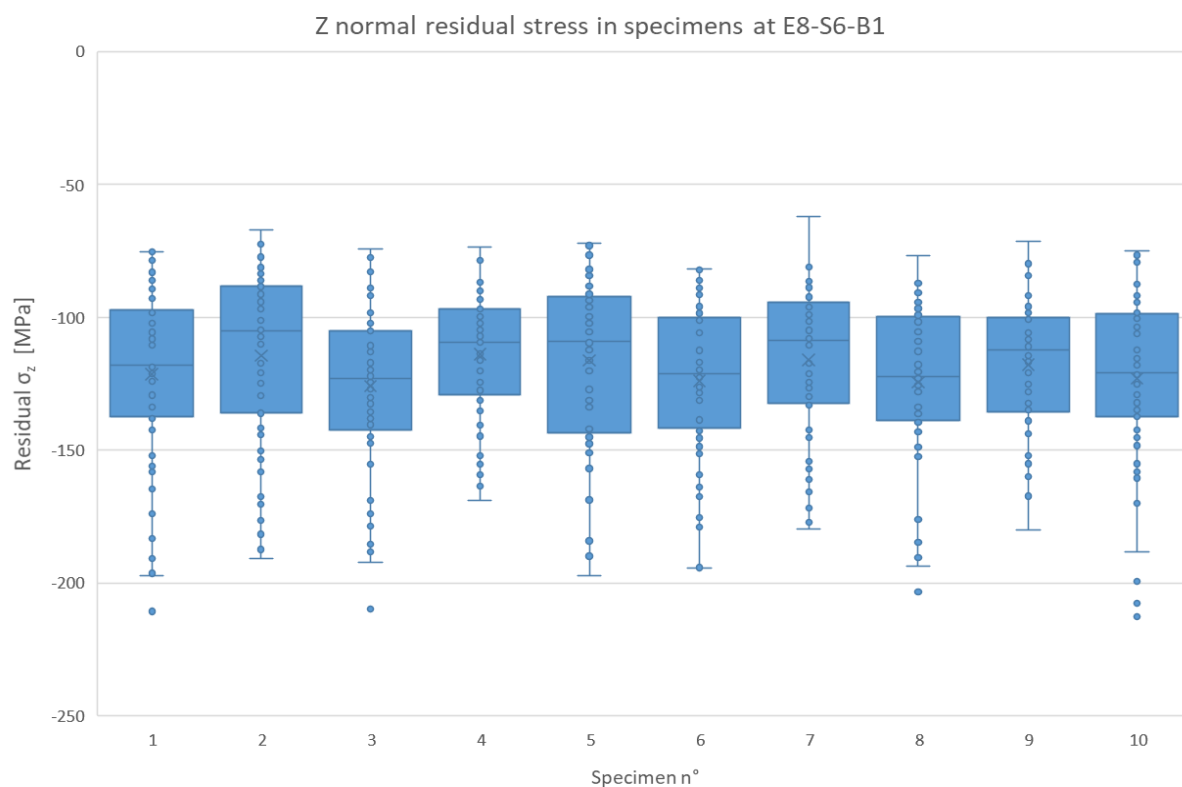
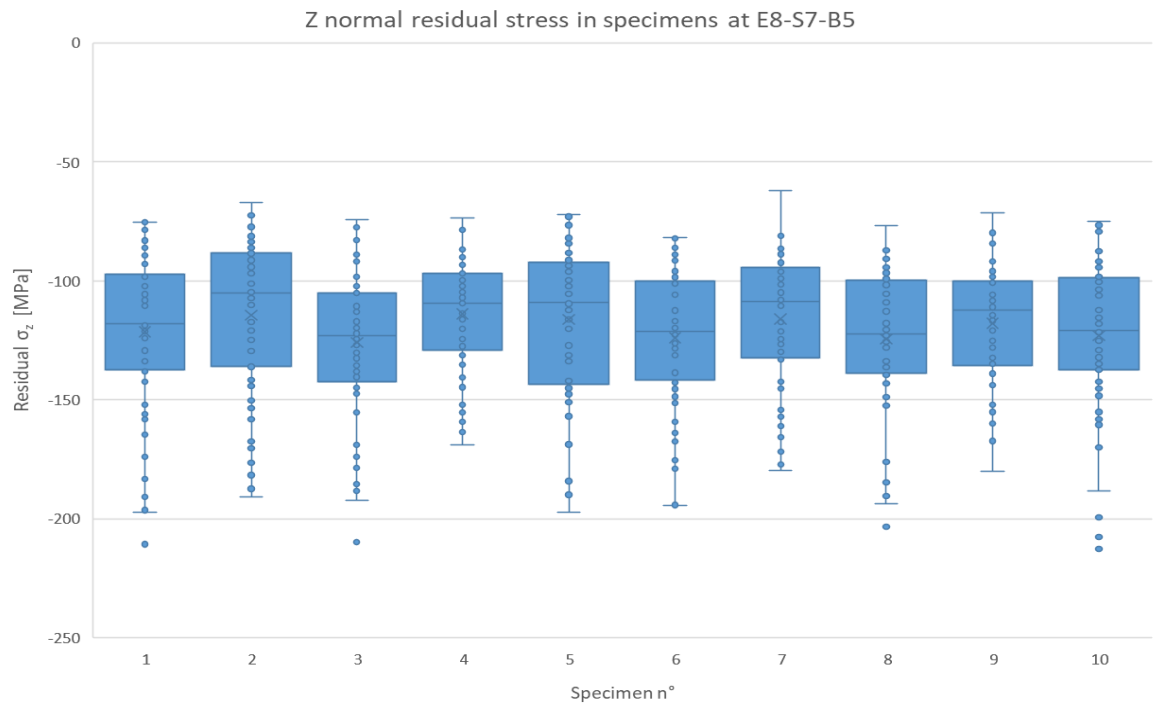
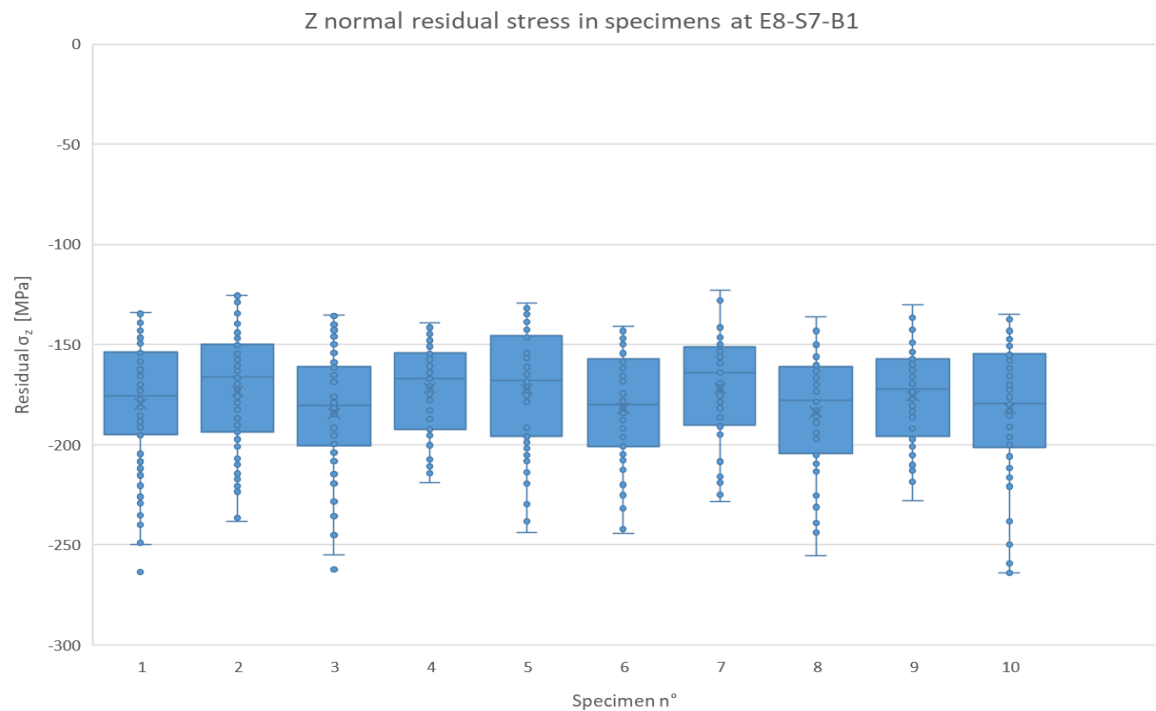


Fig. 6.6: Boxplot of residual σ_z at E8-S6-B1

**Fig. 6.7: Boxplot of residual σ_z at E8-S7-B5****Fig. 6.8: Boxplot of residual σ_z at E8-S7-B1**

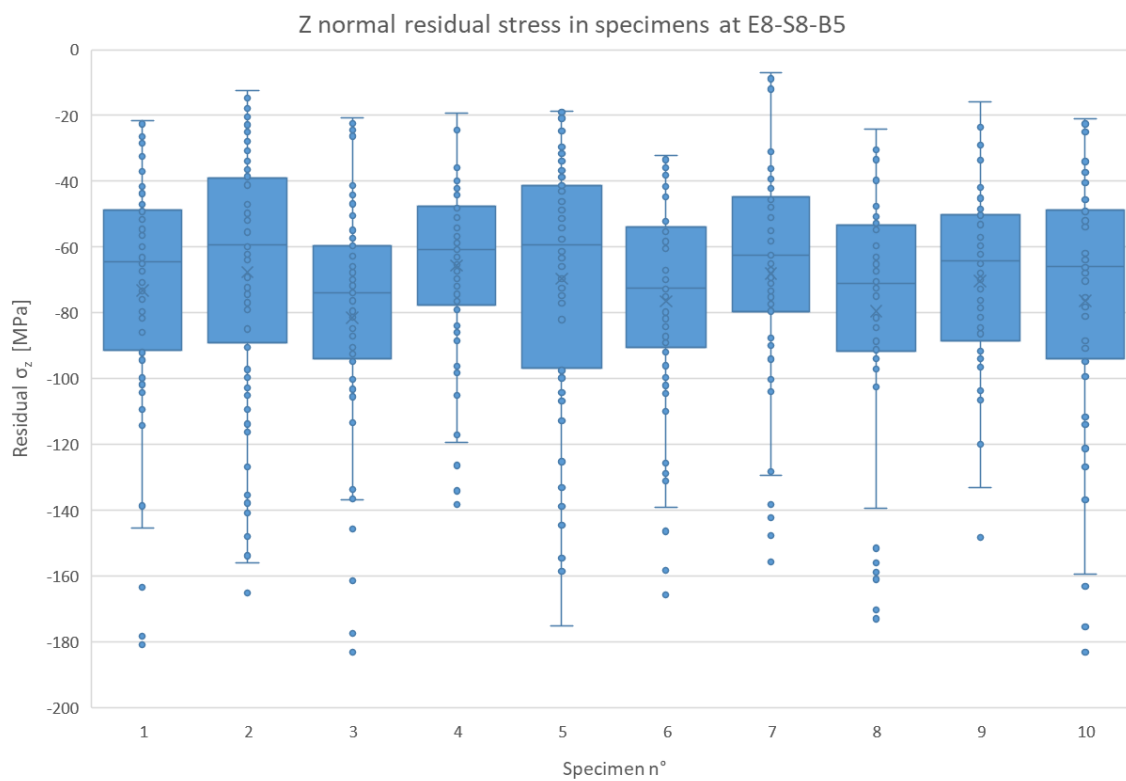


Fig. 6.9: Boxplot of residual σ_z at E8-S8-B5

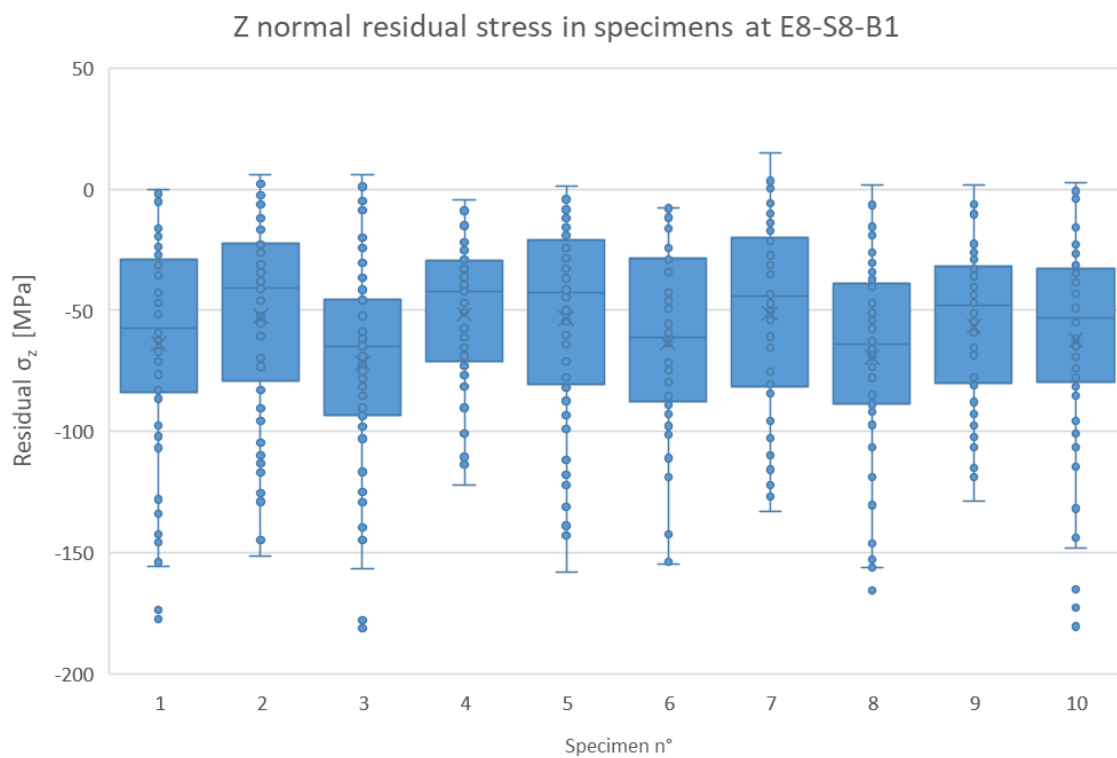
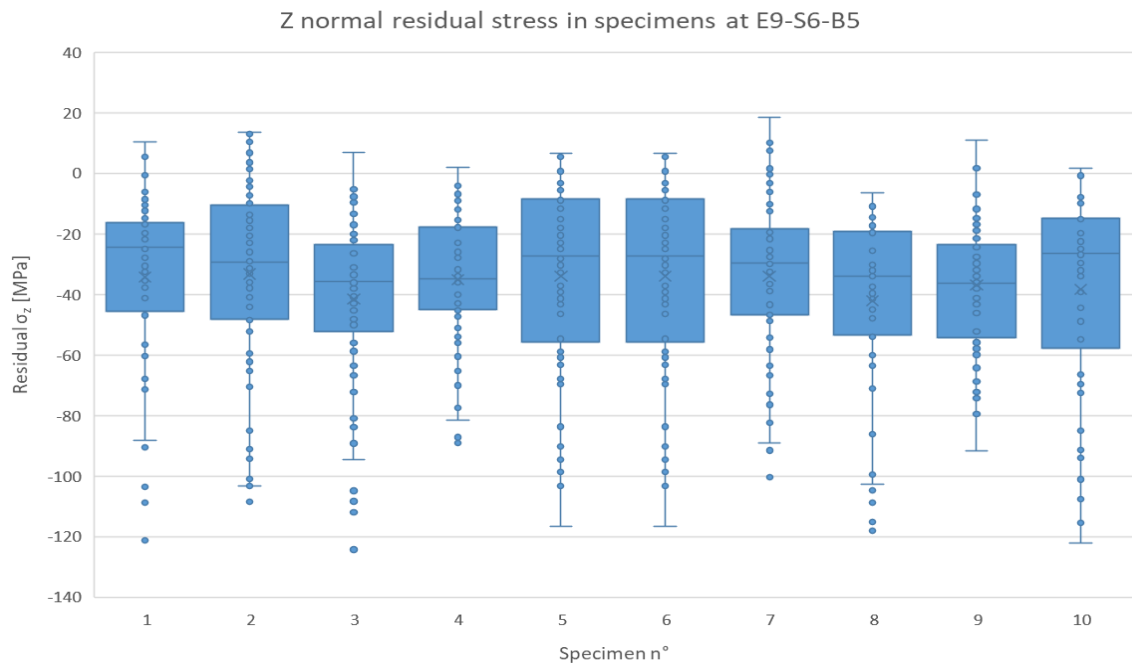
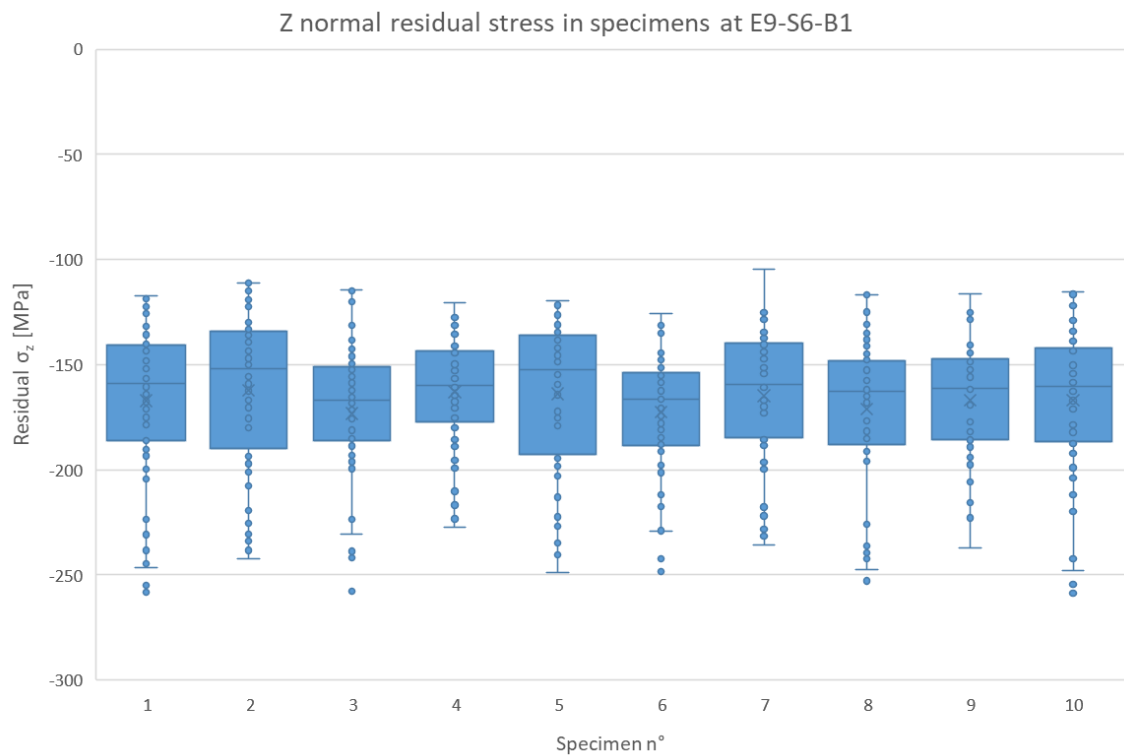


Fig. 6.10: Boxplot of residual σ_z at E8-S8-B1

**Fig. 6.11: Boxplot of residual σ_z at E9-S6-B5****Fig. 6.12: Boxplot of residual σ_z at E9-S6-B1**

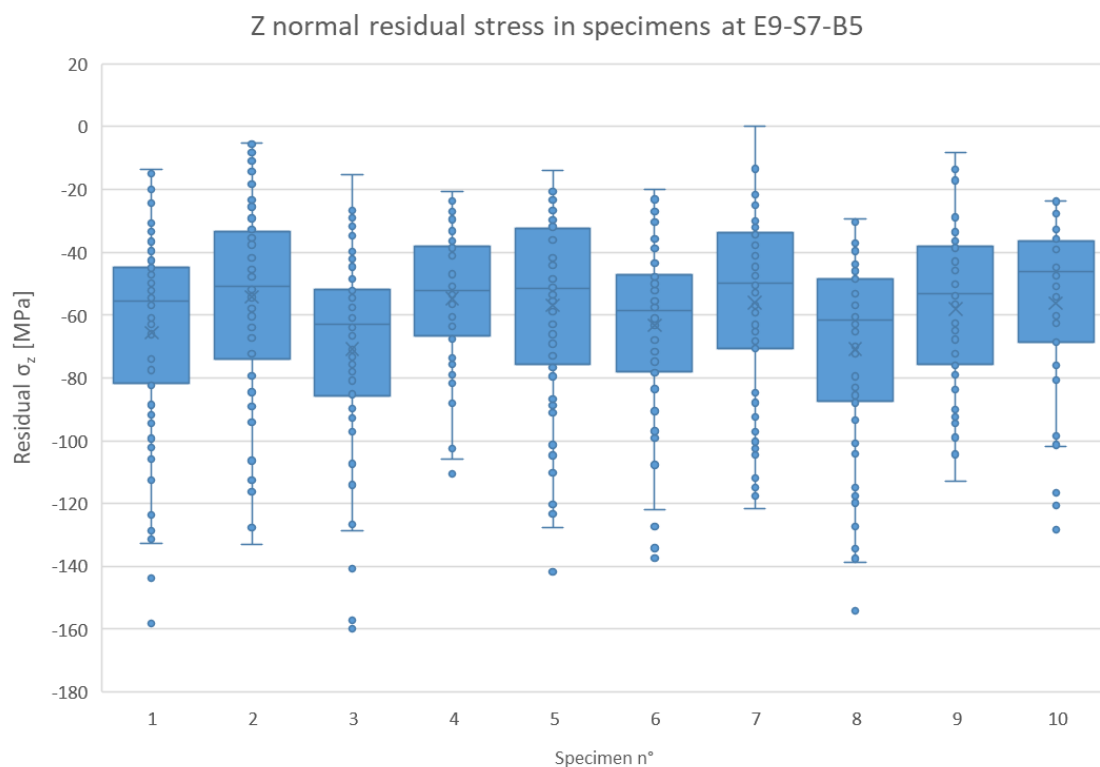


Fig. 6.13: Boxplot of residual σ_z at E9-S7-B5

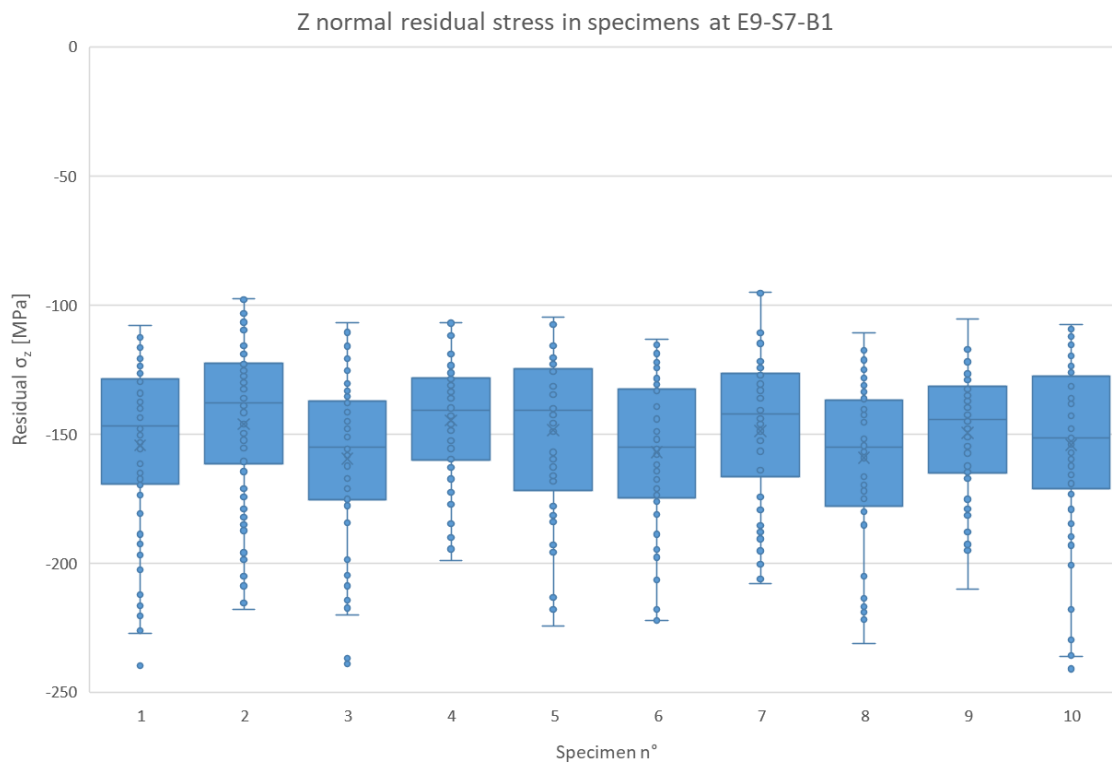
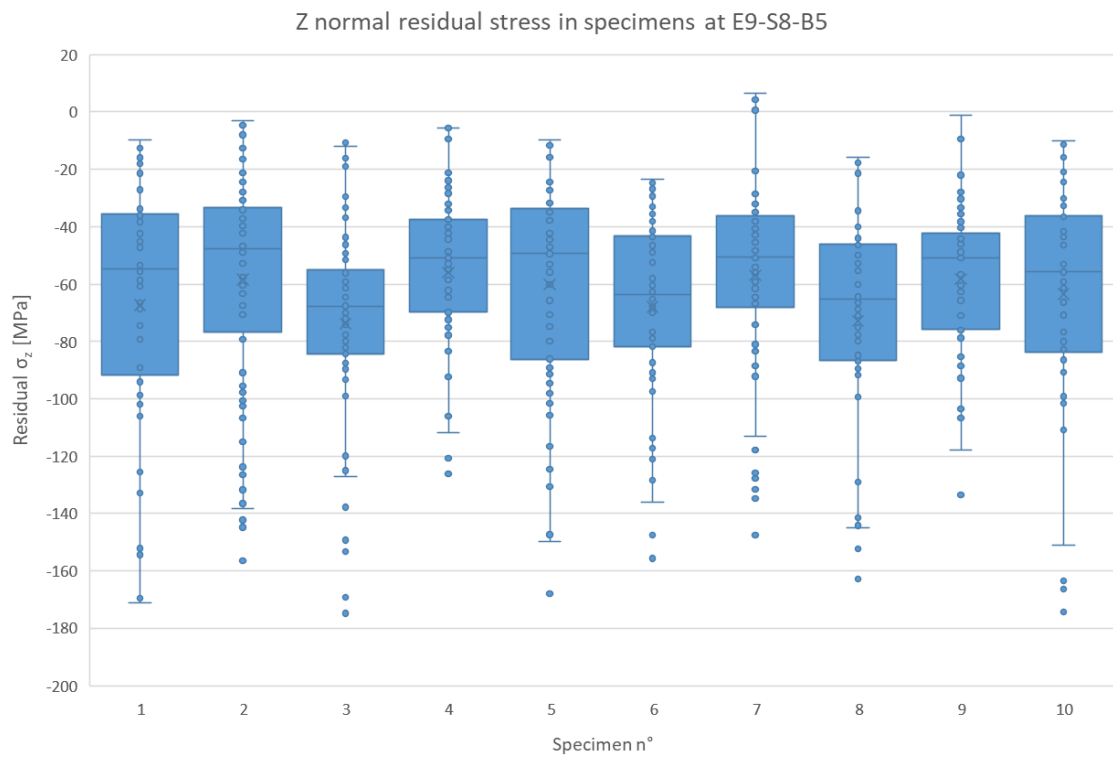
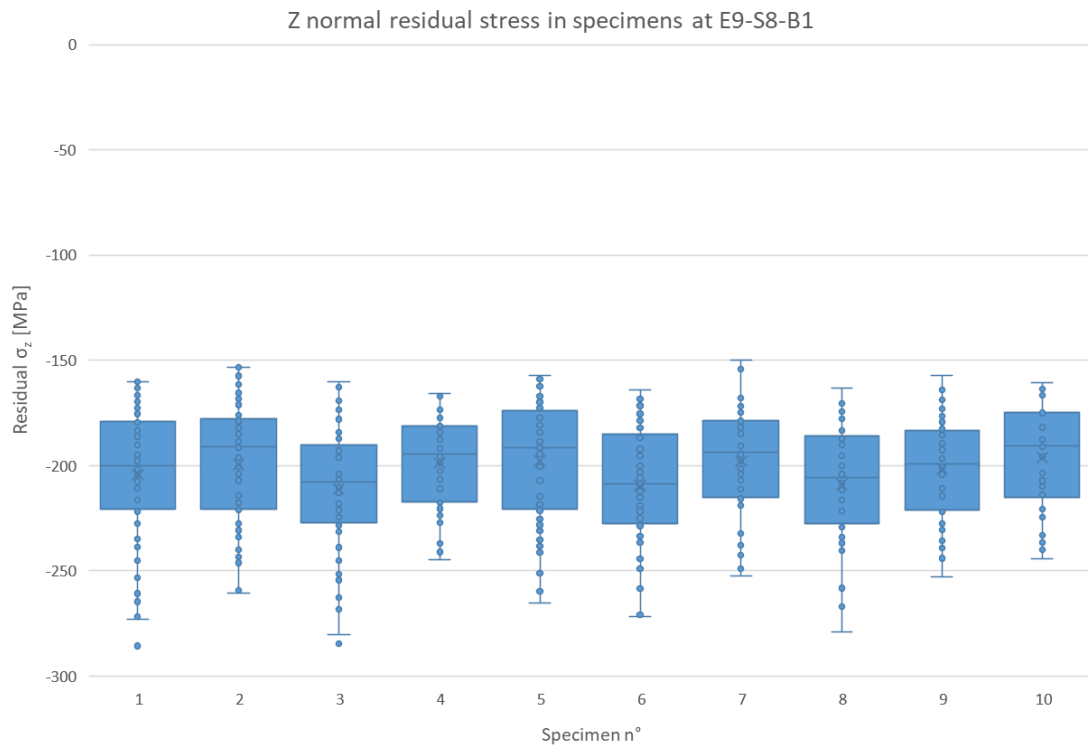


Fig. 6.14: Boxplot of residual σ_z at E9-S7-B1

**Fig. 6.15: Boxplot of residual σ_z at E9-S8-B5****Fig. 6.16: Boxplot of residual σ_z at E9-S8-B1**

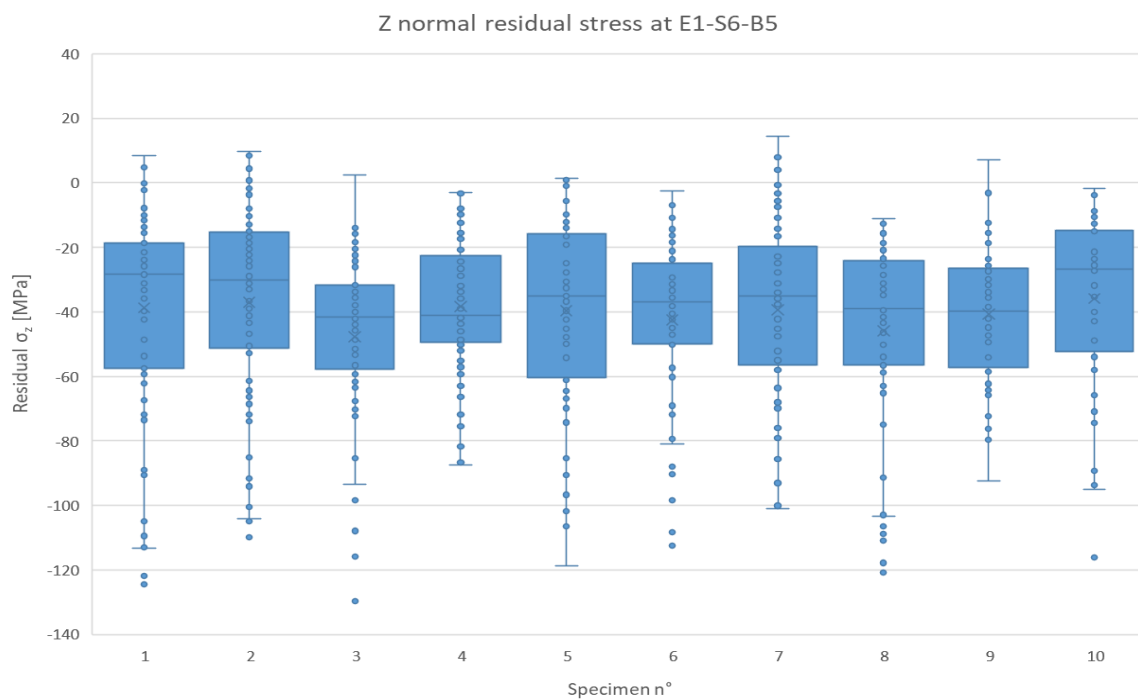


Fig. 6.17: Boxplot of residual σ_z at E1-S6-B5

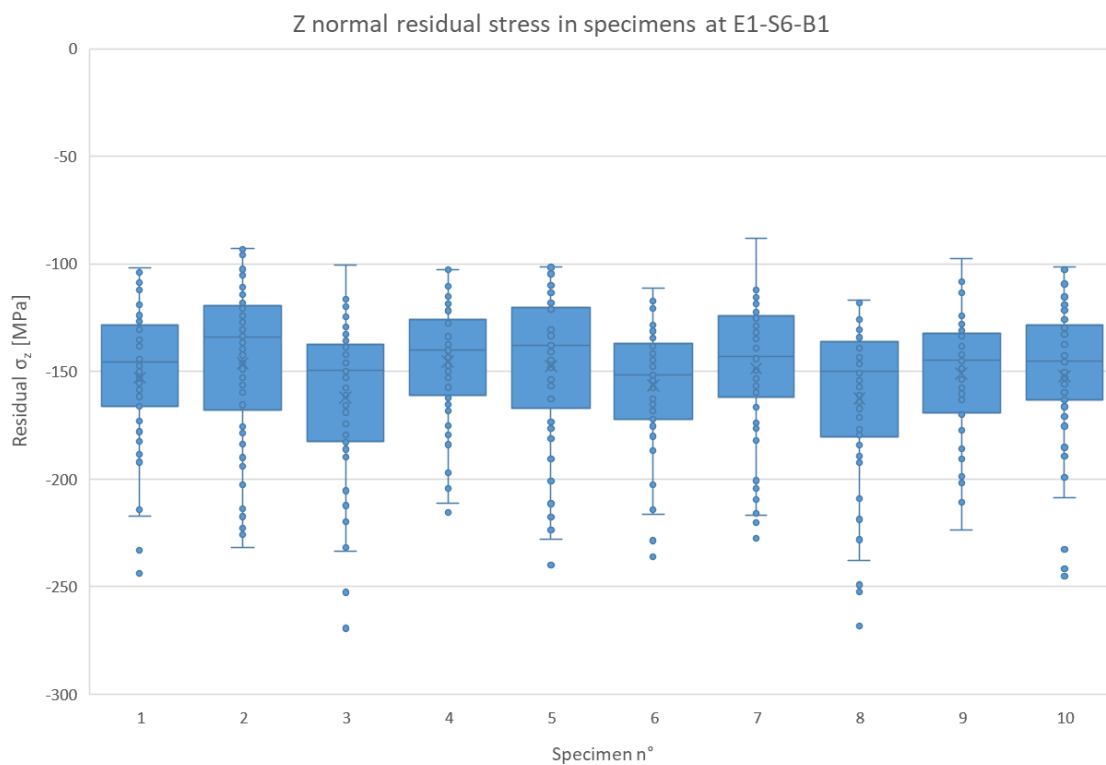
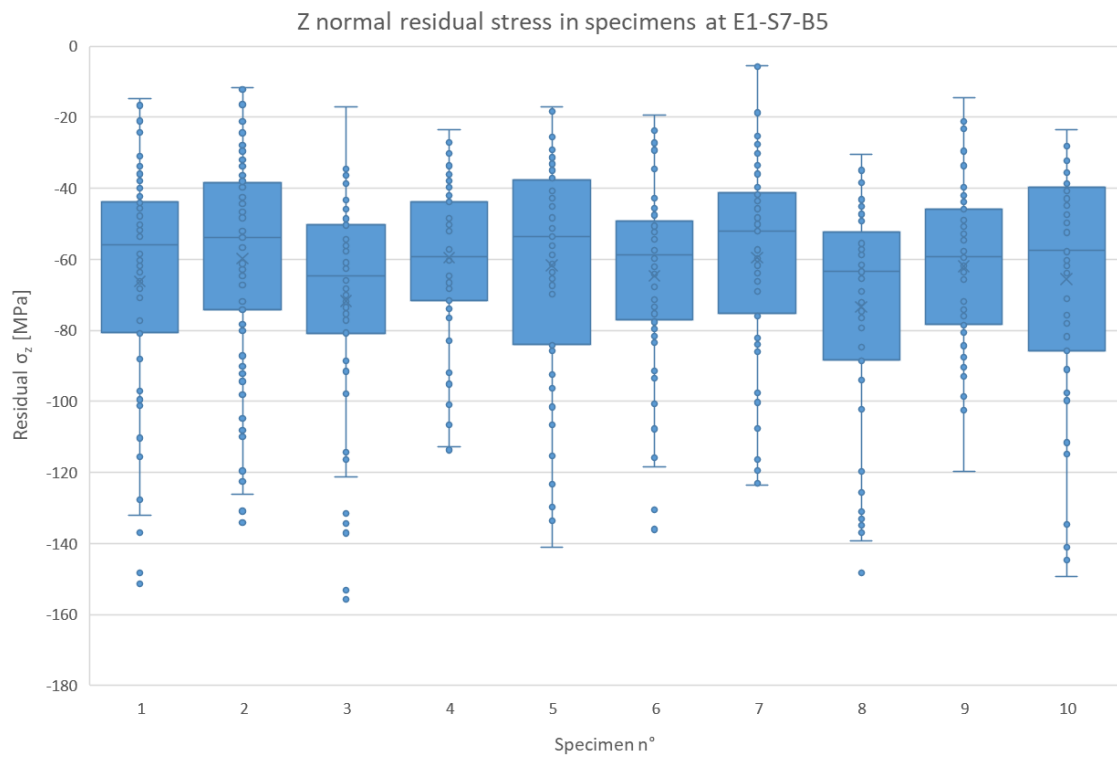
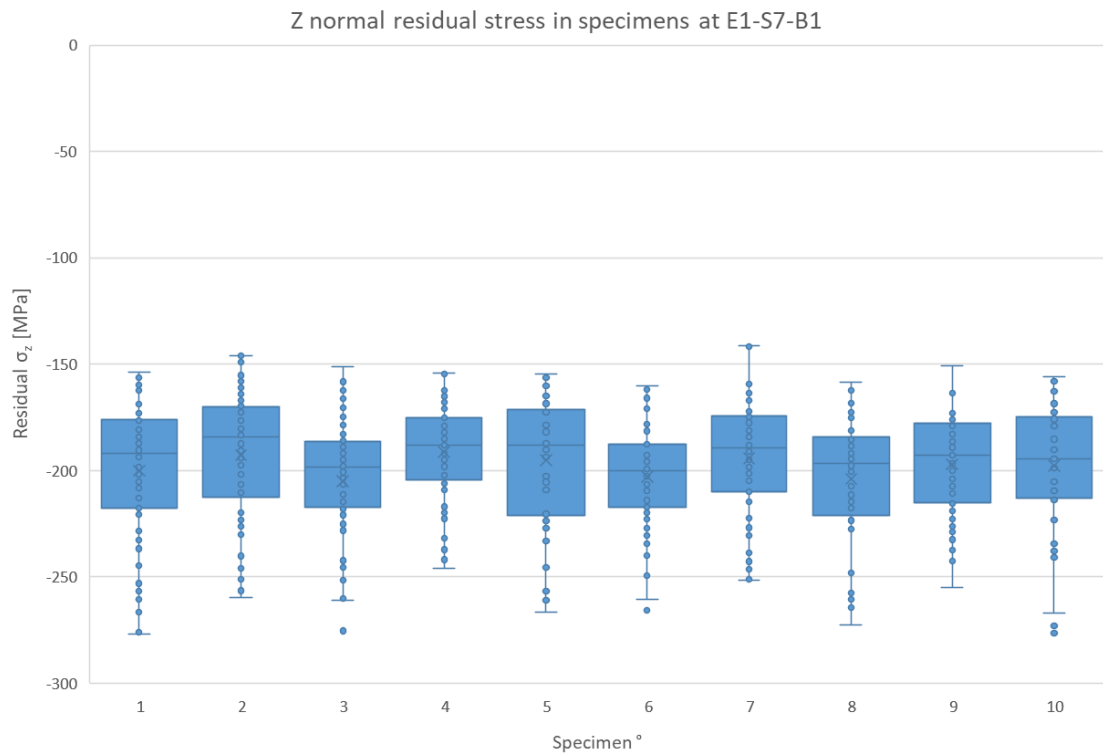


Fig. 6.18: Boxplot of residual σ_z at E1-S6-B1

**Fig. 6.19: Boxplot of residual σ_z at E1-S7-B5****Fig. 6.20: Boxplot of residual σ_z at E1-S7-B1**

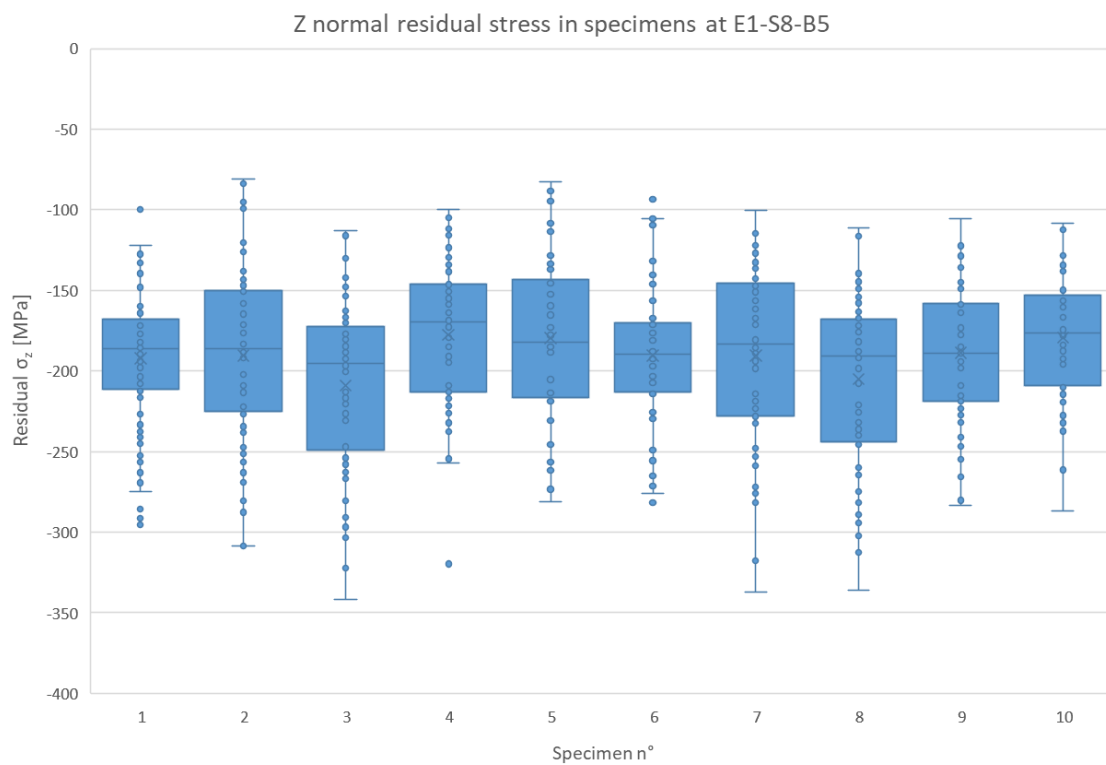


Fig. 6.21: Boxplot of residual σ_z at E1-S8-B5

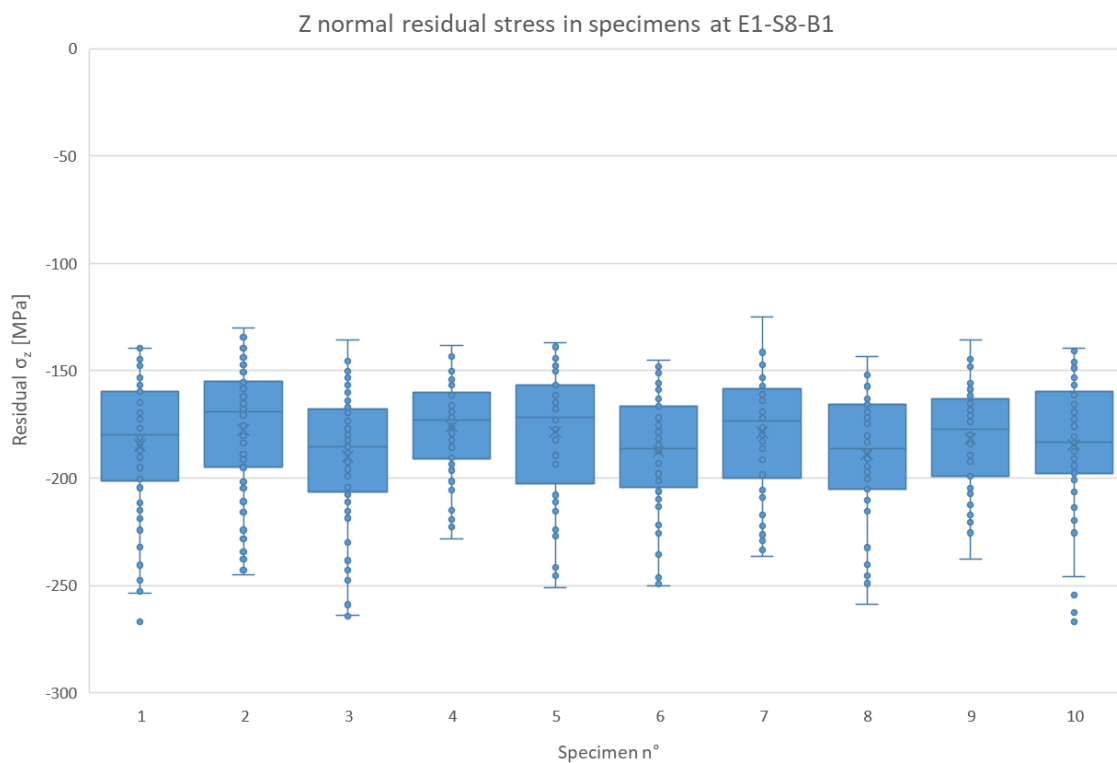


Fig. 6.22: Boxplot of residual σ_z at E1-S8-B1

As it can be seen, there is a variability in the specimens and also in its voxel nodes but the means of them are close and not so many outlier points were found. The distribution seems normal or similar and most of the measured points of each specimen are close to the mean.

A graph was done to sum up the data obtained in the simulation (Fig. 6.23). As we can see there is a big difference between the values of beam width. An effect of the scan speed can also be seen when the beam width value is 50 μm , the higher the speed the lower the residual stresses. However, it is not the case when the beam width is 100 μm . For a deep understanding and a better comprehension, in the next page the regression analysis of Minitab, its residual plots and the effects of the significant variables can be seen (Fig. 6.24)(Fig. 6.25)(Fig. 6.26). There, the beam width and scanning speed are significant parameters with a p-value of 0,001 and 0,000. Neither the interactions between the parameters nor efficiency were found significant in other models and were not displayed. The higher the beam width, the less compressive the residual stresses are and the lower the scan speed the less compressive stress. The R-square found for the regression found was 96,02% and the adjusted one 95%. The residual plots validate the regression model.

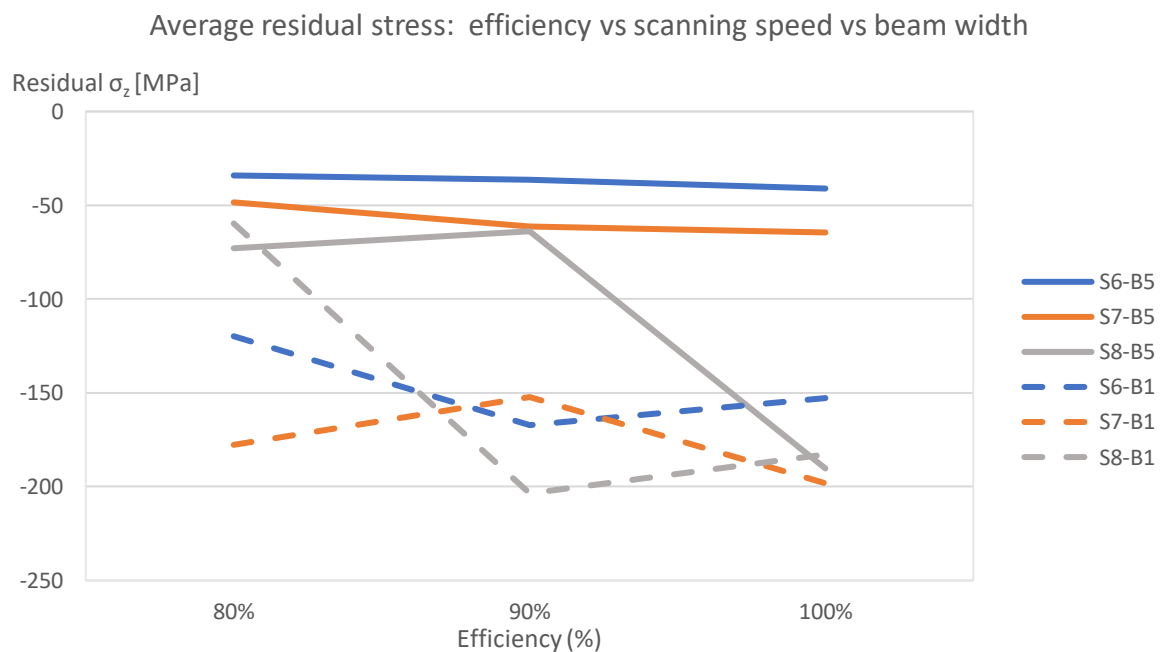


Fig. 6.23: Efficiency, scanning speed and beam width effect in residual stress

Regression Analysis: Residual Stress versus Speed, Beam ... , Efficiency

Analysis of Variance

Source	DF	Adj SS	Adj MS	F-Value	P-Value
Regression	3	58624.8	19541.6	96.40	0.000
Speed	1	3854.7	3854.7	19.02	0.001
Beam width	1	51293.0	51293.0	253.03	0.000
Efficiency	1	502.4	502.4	2.48	0.141
Error	12	2432.6	202.7		
Total	15	61057.4			

Model Summary

S	R-sq	R-sq(adj)	R-sq(pred)
14.2379	96.02%	95.02%	92.73%

Coefficients

Term	Coef	SE Coef	T-Value	P-Value	VIF
Constant	262.3	51.5	5.09	0.000	
Speed	-0.1988	0.0456	-4.36	0.001	1.00
Beam width	-22.94	1.44	-15.91	0.000	1.03
Efficiency	-71.8	45.6	-1.57	0.141	1.03

Regression Equation

Residual Stress = 262.3 - 0.1988 Speed - 22.94 Beam width - 71.8 Efficiency

Fits and Diagnostics for Unusual Observations

Obs	Residual Stress	Fit	Resid	Std Resid
2	-119.81	-143.80	23.99	2.06 R

R Large residual

Residual Plots for Residual Stress

Fig. 6.24: General factorial regression of residual stress with MINITAB

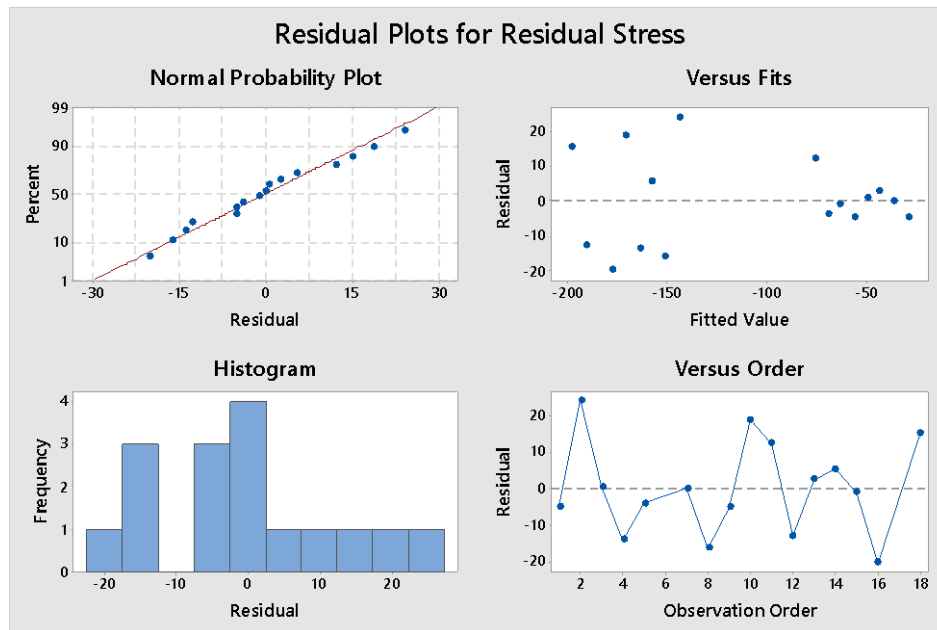


Fig. 6.25: Residual plots of the residual stress regression

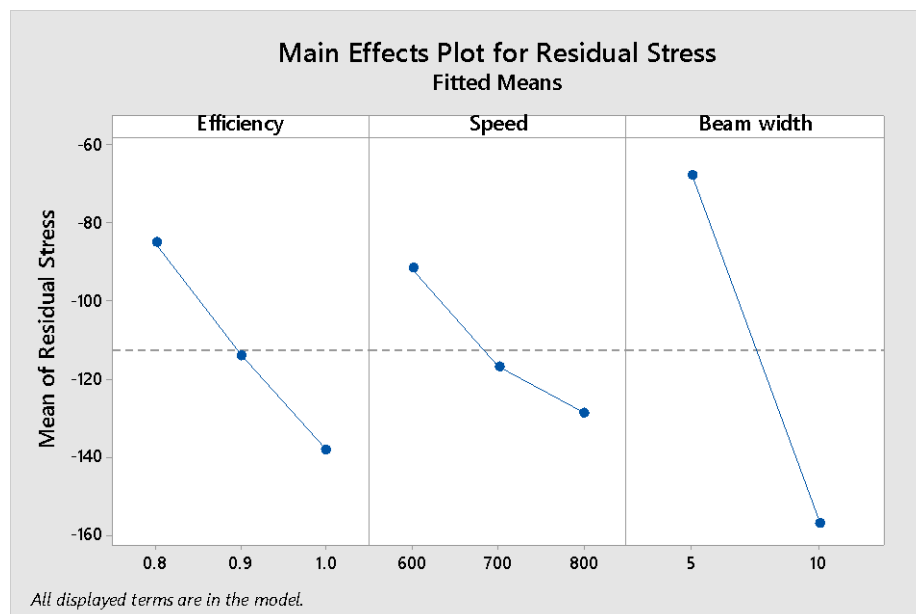


Fig. 6.26: Effects of individual parameters on residual stress

The results for every plot of energy density vs residual stress and scan rate vs residual stress are shown in a graphic (Fig. 6.27) (Fig. 6.28). There are only two points that do not fit into the regression. Correlation test was also performed with and without them (Fig. 6.29) (Fig. 6.30). Without these two points the p-values are 0. However, with all the points only scan rate is significant with a p-value of 0.001. The graphs show that the high the scan rate the more compressive residual stresses, Moreover, the more energy density, the less compressive stress.

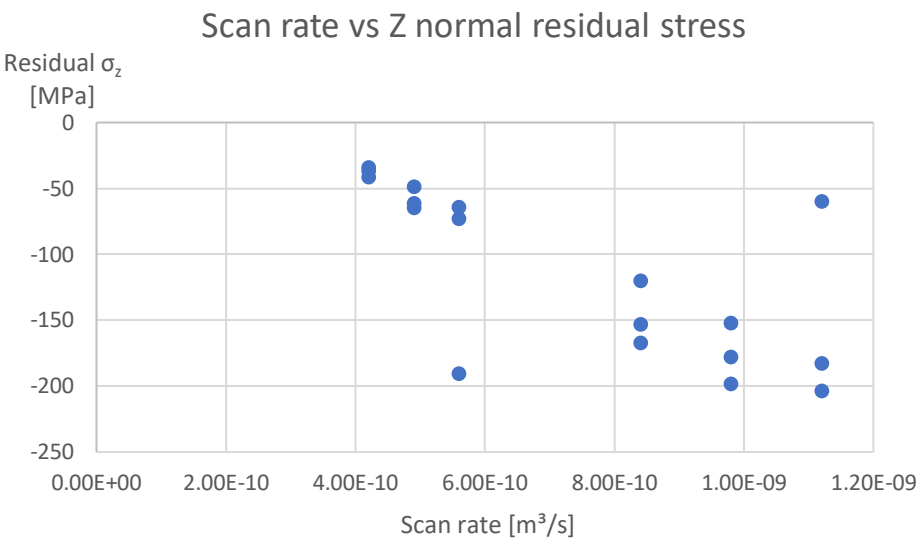


Fig. 6.27: Residual σ_z vs scan rate

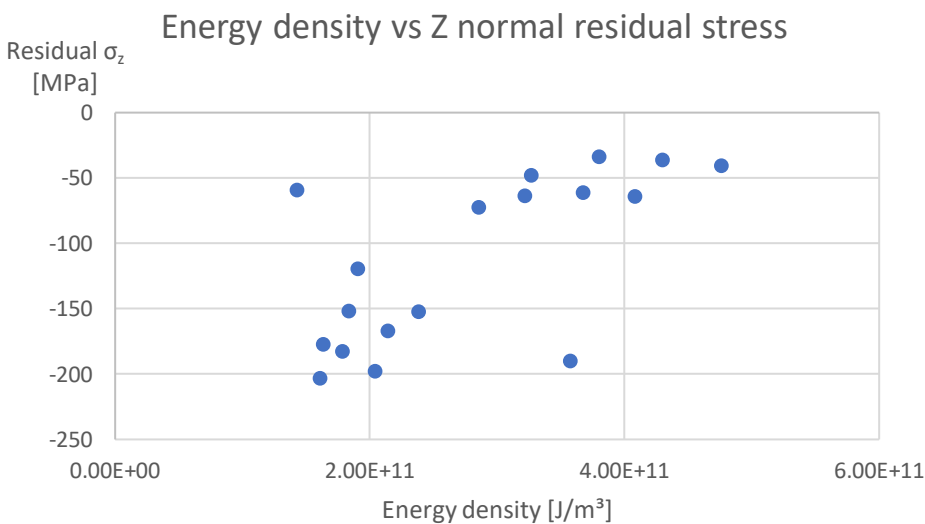


Fig. 6.28: Residual σ_z vs energy density

Correlation: Residual Stress, Energy density Correlation: Residual stress, Scan rate

Correlations		Correlations	
Pearson correlation	0.458	Pearson correlation	-0.724
P-value	0.056	P-value	0.001

Fig. 6.29: Residual σ_z correlation test with scan rate and energy density

Correlation: Residual stress, Energy density Correlation: Residual stress, Scan rate

Correlations

Pearson correlation 0.903
P-value 0.000

Correlations

Pearson correlation -0.973
P-value 0.000

Fig. 6.30: Residual σ_z correlation test with scan rate and energy density after removing biased points

6.1.2 Distortion

The next three pictures show the differences of distortion between the layout simulation with default material data (Fig. 6.31), with new material data added without heat treatment (Fig. 6.32) and with heat treatment (Fig. 6.33). Also, the evolution of the maximum distortion and minimum distortion average with default data, new data added and heat treatment (Fig. 6.34) is showed:

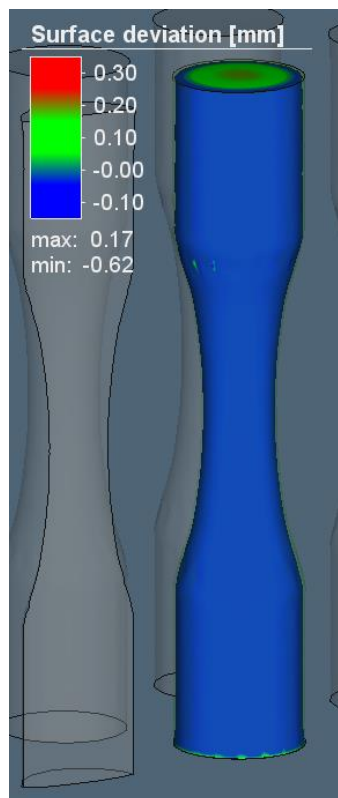


Fig. 6.31: Distortion in specimens with default data

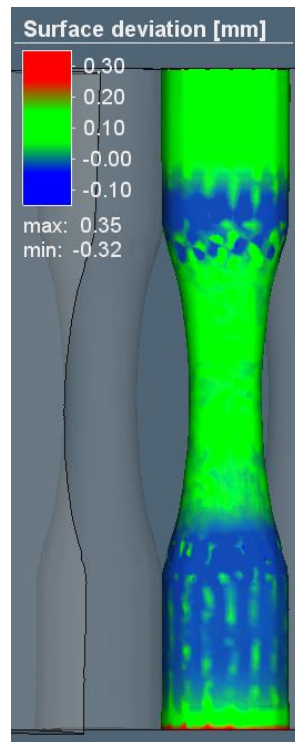


Fig. 6.32: Distortion in specimens with new data and without heat treatment

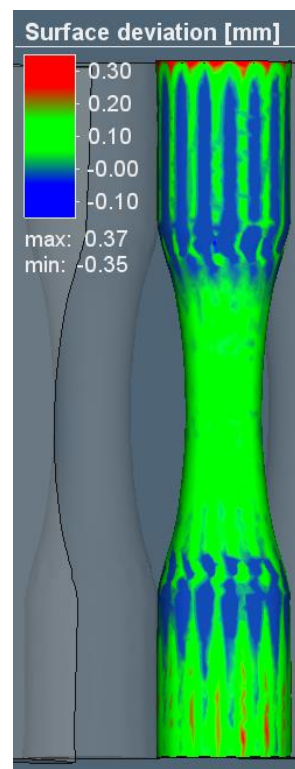


Fig. 6.33: Distortion in specimens with new data and heat treatment

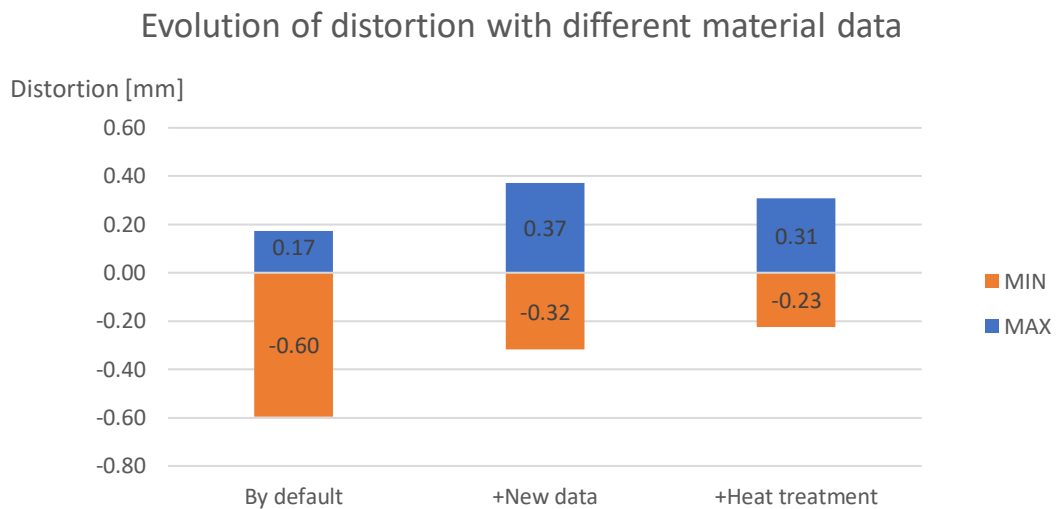


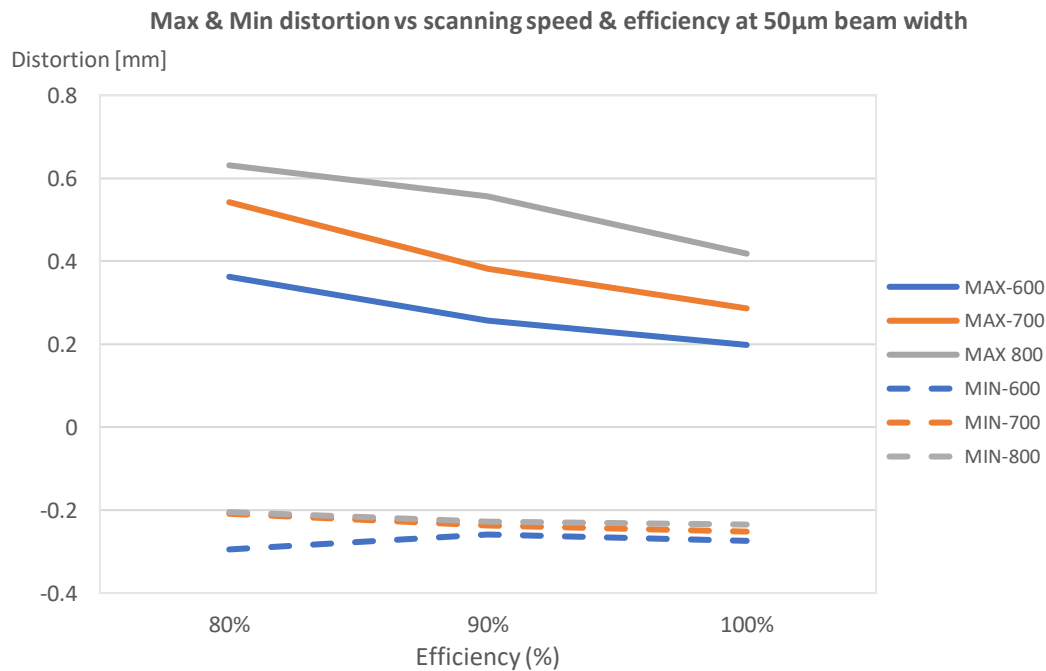
Fig. 6.34: Evolution of maximum and minimum distortion average with material data added

With the new material data added the distortions change like in the single specimen case. Whereas with the material default data the distortions are mainly negative, with the new data added and the heat treatment the distortions are mainly positive. This change can also be seen with the maximum and minimum distortion. A big difference is observed between the material added and the default data. With the heat treatment, maximum and minimum distortions are reduced.

The next table (Table 6.2) shows the maximum and the minimum distortions measured in all the sensitivity study simulations. In addition, energy density and scan rate parameter values are also showed. The results are plot in 2 graphs, one with 50 μm beam width (Fig. 6.35) and the other with 100 μm (Fig. 6.36):

Simulation name	Parameters			Results		Internal parameters	
	Efficiency (%)	Scanning Speed [mm/s]	Beam Width [μm]	Min distortion [mm]	Max distortion [mm]	Energy density [J/m^3]	Scan rate [m^3/s]
E8-S6-B5	80	600	50	-0,30	0,36	3,80E+11	4,20E-10
E9-S6-B5	90	600	50	-0,26	0,54	4,30E+11	4,20E-10
E1-S6-B5	100	600	50	-0,28	0,63	4,76E+11	4,20E-10
E8-S7-B5	80	700	50	-0,21	0,71	3,27E+11	4,90E-10
E9-S7-B5	90	700	50	-0,24	0,66	3,67E+11	4,90E-10
E1-S7-B5	100	700	50	-0,25	0,62	4,08E+11	4,90E-10
E8-S8-B5	80	800	50	-0,21	0,26	2,86E+11	5,60E-10
E9-S8-B5	90	800	50	-0,23	0,38	3,21E+11	5,60E-10
E1-S8-B5	100	800	50	-0,24	0,56	3,57E+11	5,60E-10
E8-S6-B1	80	600	100	-0,16	0,65	1,90E+11	8,40E-10
E9-S6-B1	90	600	100	-0,17	0,74	2,14E+11	8,40E-10
E1-S6-B1	100	600	100	-0,20	0,66	2,38E+11	8,40E-10
E8-S7-B1	80	700	100	-0,17	0,20	1,63E+11	9,80E-10
E9-S7-B1	90	700	100	-0,16	0,29	1,84E+11	9,80E-10
E1-S7-B1	100	700	100	-0,16	0,42	2,04E+11	9,80E-10
E8-S8-B1	80	800	100	-0,20	0,63	1,43E+11	1,12E-09
E9-S8-B1	90	800	100	-0,18	0,68	1,61E+11	1,12E-09
E1-S8-B1	100	800	100	-0,16	0,72	1,79E+11	1,12E-09

Table 6.2: max and min distortion sensitivity study results table

Fig. 6.35: Max and Min distortion vs scanning speed and efficiency at 50 μm beam width

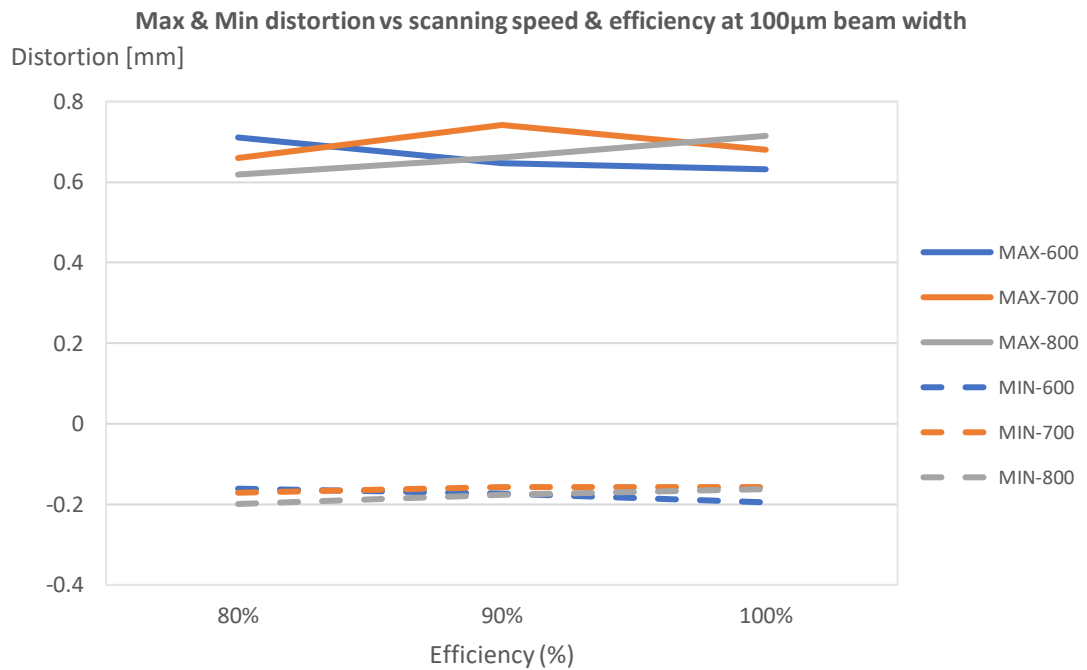


Fig. 6.36: Max and Min distortion vs scanning speed and efficiency at 100 μ m beam width

We can see clearly a pattern in the graph of 50 μ m. While the maximum distortions become bigger at less efficiency and the higher the scan speed, minimum distortions are bigger when the scan speed is lower and also it could be when the higher the efficiency is. Nevertheless, when the beam width is 100 μ m no pattern can be seen. To solve this a regression was performed to understand if the parameters are significant in the maximum and minimum distortion. Both regression models show that efficiency, scan speed and beam width are significant parameters to the maximum and the minimum distortion.

Regarding the maximum distortion, the regression (Fig. 6.37) fits with a R-square of 87,2% and a R-square adjusted of 85%. The p-values of the parameters are smaller (very close to 0). The residual plots do not show any outlier (Fig. 6.38). Moreover, the effect of the parameters in the maximum distortion show that scanning speed and beam width increase the maximum distortion when they are higher. Oppositely, the efficiency reduces the maximum distortion when it is at high levels. This fact can be seen in Fig. 6.39.

In the minimum distortion the pattern is the same. the regression (Fig. 6.37) fits with a R-square of 91,6% and a R-square adjusted of 89,5%. The p-values of the parameters are smaller (less than 0,01). The residual plots do not show any outlier (Fig. 6.38). Moreover, the effect of the parameters in the minimum distortion show that scanning speed and beam width reduces the minimum distortion when they are higher. Oppositely, the efficiency increases the negative distortion when it is at high levels.

Regression Analysis: MAX versus Efficiency, Speed, Beam width

Analysis of Variance

Source	DF	Adj SS	Adj MS	F-Value	P-Value
Regression	3	0.44539	0.148464	29.53	0.000
Efficiency	1	0.05183	0.051832	10.31	0.007
Speed	1	0.07934	0.079335	15.78	0.002
Beam width	1	0.36844	0.368441	73.28	0.000
Error	13	0.06537	0.005028		
Total	16	0.51076			

Model Summary

S	R-sq	R-sq(adj)	R-sq(pred)
0.0709090	87.20%	84.25%	77.45%

Coefficients

Term	Coef	SE Coef	T-Value	P-Value	VIF
Constant	0.130	0.239	0.54	0.596	
Efficiency	-0.694	0.216	-3.21	0.007	1.02
Speed	0.000859	0.000216	3.97	0.002	1.02
Beam width	0.05939	0.00694	8.56	0.000	1.01

Regression Equation

MAX = 0.130 - 0.694 Efficiency + 0.000859 Speed + 0.05939 Beam width

Fits and Diagnostics for Unusual Observations

Obs	MAX	Fit	Resid	Std Resid
12	0.6610	0.7863	-0.1253	-2.04 R

R Large residual

Residual Plots for MAX

Fig. 6.37: General regression of Maximum distortion with MINITAB

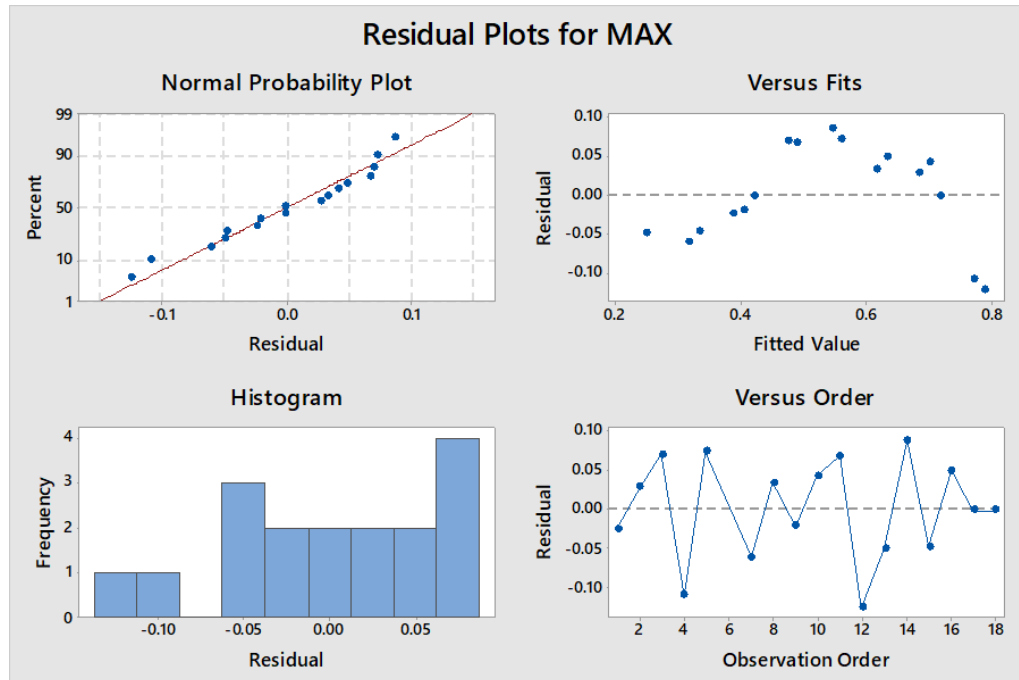


Fig. 6.38: Residual plots of maximum distortion regression

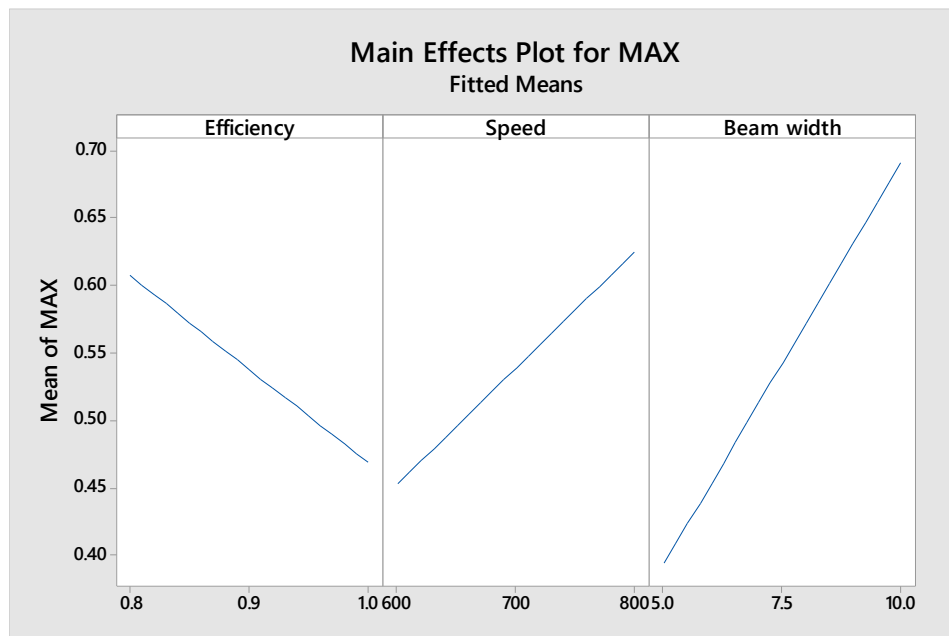


Fig. 6.39: Effects of individual parameters in maximum distortion

Regression Analysis: MIN versus Efficiency, Speed, Beam width

Analysis of Variance

Source	DF	Adj SS	Adj MS	F-Value	P-Value
Regression	3	0.021949	0.007316	43.67	0.000
Efficiency	1	0.001564	0.001564	9.34	0.010
Speed	1	0.001615	0.001615	9.64	0.009
Beam width	1	0.020060	0.020060	119.74	0.000
Error	12	0.002010	0.000168		
Total	15	0.023959			

Model Summary

S	R-sq	R-sq(adj)	R-sq(pred)
0.0129430	91.61%	89.51%	85.03%

Coefficients

Term	Coef	SE Coef	T-Value	P-Value	VIF
Constant	-0.2853	0.0497	-5.74	0.000	
Efficiency	-0.1267	0.0415	-3.06	0.010	1.00
Speed	0.000129	0.000041	3.11	0.009	1.03
Beam width	0.01434	0.00131	10.94	0.000	1.03

Regression Equation

MIN = -0.2853 - 0.1267 Efficiency + 0.000129 Speed + 0.01434 Beam width

Fits and Diagnostics for Unusual Observations

Obs	MIN	Fit	Resid	Std Resid
12	-0.17600	-0.15294	-0.02306	-2.07 R

R Large residual

Residual Plots for MIN

Fig. 6.40: General regression of Minimum distortion with MINITAB

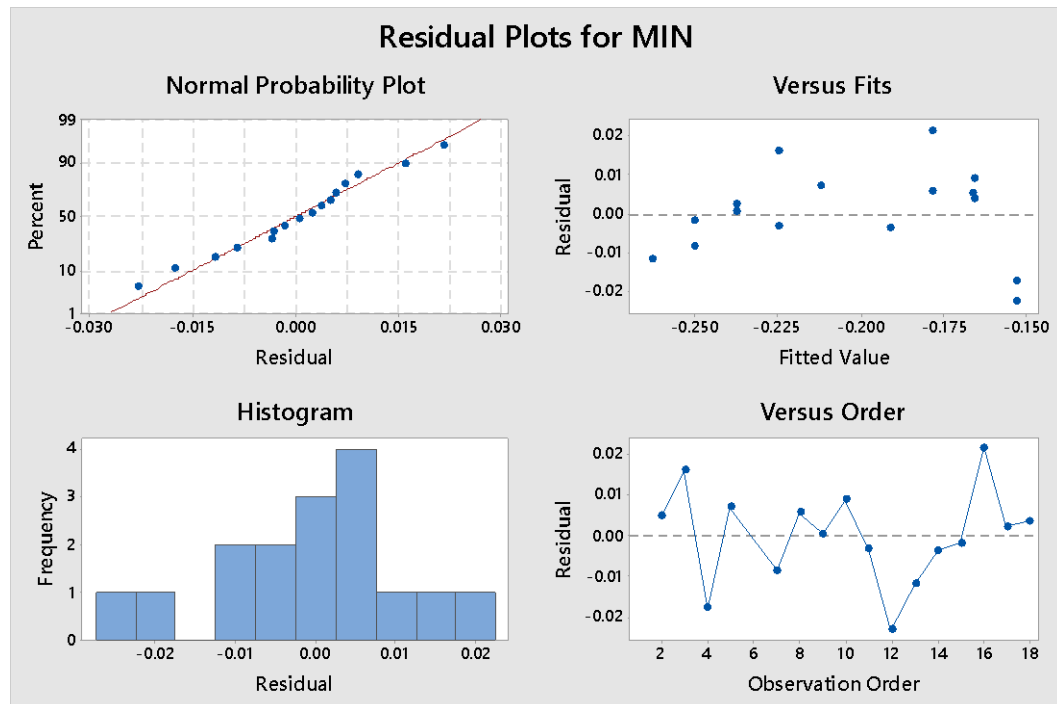


Fig. 6.41: Residual plots of the minimum distortion regression

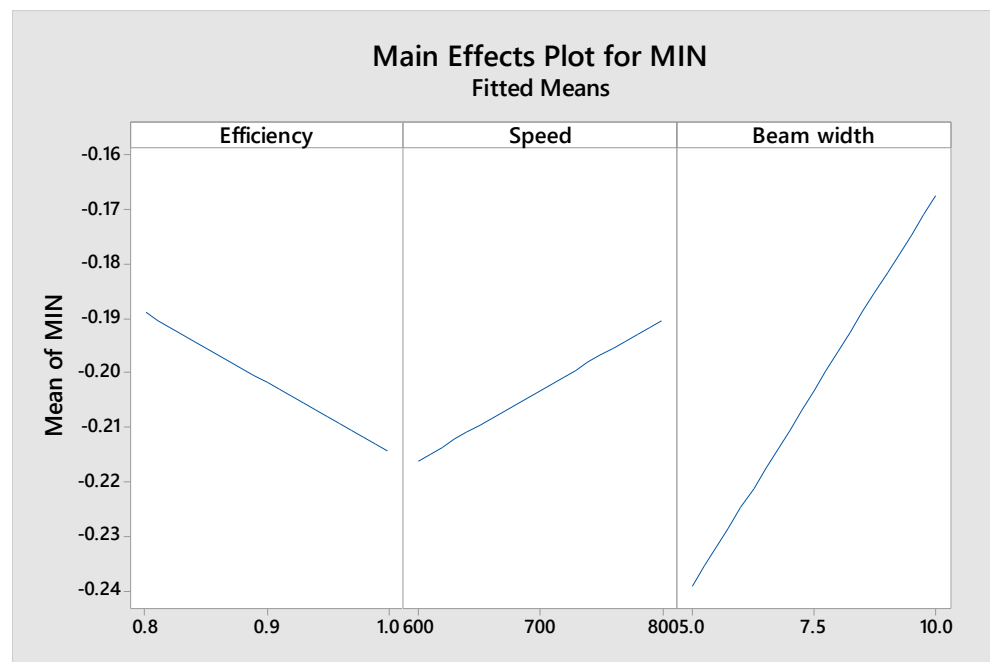


Fig. 6.42: Effects of individual parameters in minimum distortion

To end the distortion analysis the max and minimum value were plotted versus energy density and scan rate (Fig. 6.43)(Fig. 6.44). Regarding the maximum distortion no relation can be seen proportionally. In contrast the minimum distortion shows a proportional relation, at high levels of scan rate and at low levels of energy density, the minimum distortion becomes smaller. A

correlation test with the minimum distortion and the scan rate was done to prove it (Fig. 6.45). Nevertheless, the results show that neither energy density nor scan rate are correlated to minimum distortion.

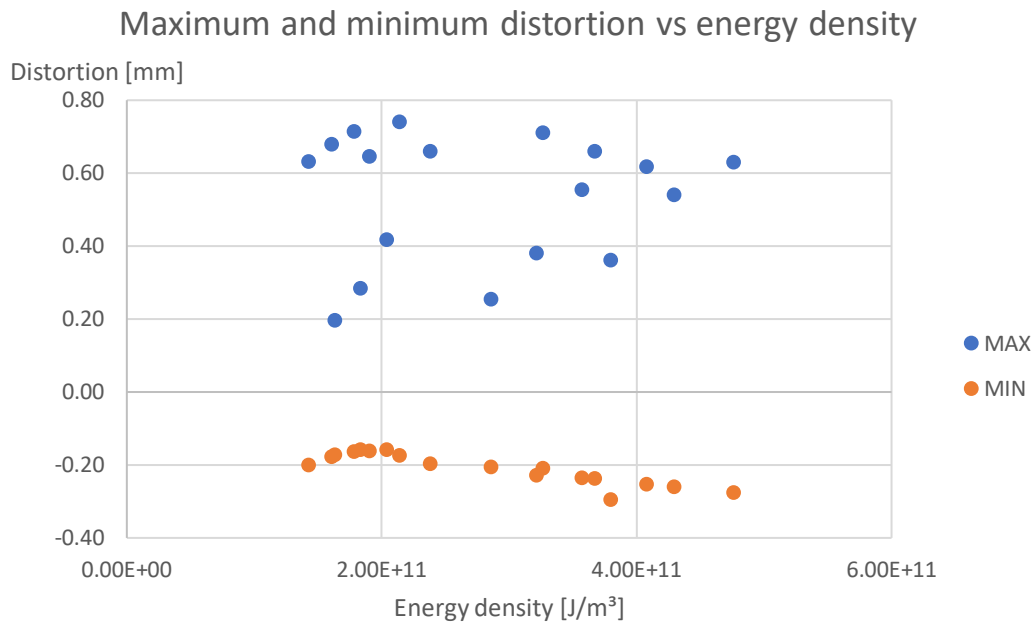


Fig. 6.43: Maximum and minimum distortion vs energy density

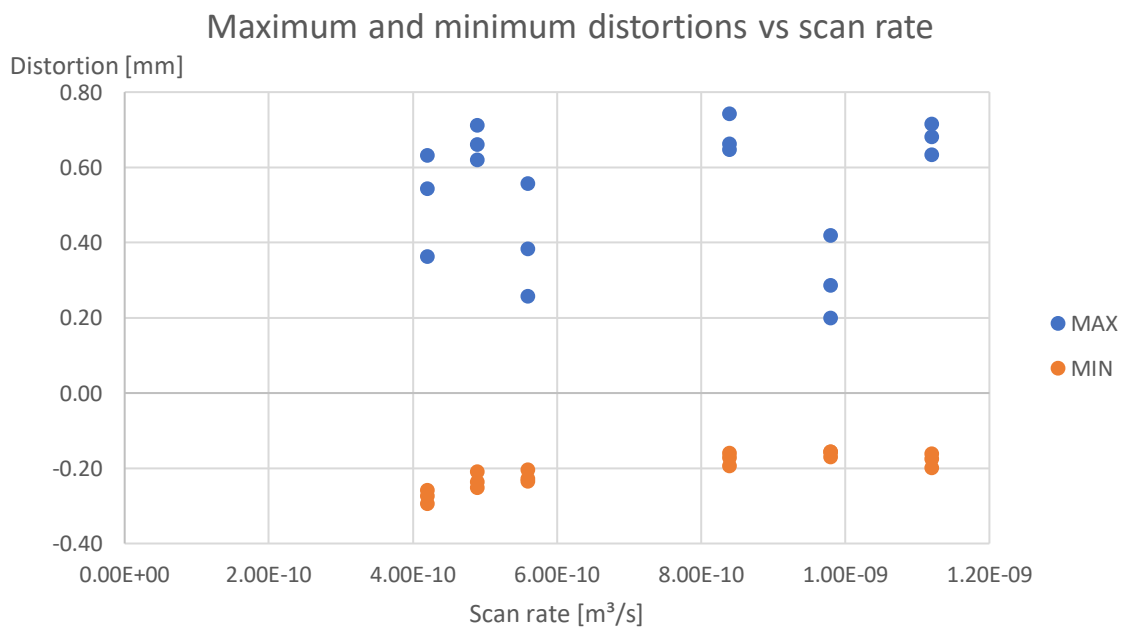


Fig. 6.44: Maximum and minimum distortion vs scan rate

Correlation: MIN, Energy density**Correlations**

Pearson correlation	0.108
P-value	0.670

Correlation: MIN, Scan rate**Correlations**

Pearson correlation	-0.106
P-value	0.676

Fig. 6.45: Correlation test of minimum distortion vs energy density and scan rate

6.2 Discussion

The comparison between default data versus the new data added simulation showed the same pattern as in the single specimen simulation. The values obtained are different respect the single specimen because there are more specimens and it reduces the heat dissipation and therefore the thermal gradient. As a result, the residual stresses are closer to zero than the single specimen simulation. However, the thermal treatment showed an unexpected effect, the residual stresses should be reduced and instead of this more compressive residual stress is induced. This could be explained maybe because the cooling rate is not the correct one chosen or Simufact performs the heat treatment with all the specimens together but the heat treatment should be performed with the specimens individually instead. The top layer and the bottom layer are also tensile and the middle regions present generally compressive Z normal residual stresses as the research paper shows[18] [23].

Regarding distortion with the new material data added there are less expansion distortion, this fact is also explained because there are more specimens manufactured at the same time and the heat flow is less than in the single specimen and therefore the expansion-compression of the specimen is less abrupt. The same pattern as seen in single specimen about residual stress and distortion is seen, the when the residual stresses are tensile, the distortion remains compressive and vice versa.

The sensitivity study performed showed that residual stresses are related to energy density, the higher the energy density the residual stresses tend to be tensile. We can relate energy density to the parameters used in the study by using Eq.(1). This results also fit with the results of the data obtained with Minitab (Fig. 6.24)(Fig. 6.26). The higher the scanning speed and the beam width, the lower the energy density and thus more compressive residual stresses. The lower the scanning speed and the beam width the higher the energy density and then the more tensile the residual stresses are. Following the Eq.(4) the efficiency should reduce the total energy applied and therefore the energy density applied. The higher the efficiency the more energy applied and more tensile residual stresses should be. The less efficiency the less energy applied and the compressive residual stresses should be. This fact is not showed in the results of Minitab (Fig. 6.24)(Fig. 6.26). Nevertheless, this value is not significant in the

regression so the effect obtained in Minitab should not be taken into account. The same reasoning but with opposite effects can be applied with the scan rate by following the Eq.(4). In order to obtain a significant effect of efficiency more simulations should be performed to obtain more data.

The sensitivity study also showed the same quantitative results in maximum and minimum distortion. The lower the efficiency and the bigger the beam width and scanning speed lead to more maximum distortion and less minimum distortion. This fact can be explained with the residual stresses, as it has been seen the combination of this parameters change the energy input. The less energy input the more compressive residual stresses are induced and as it has been seen in the single specimen simulation when there is more tensile stress there is more compressive distortion and vice versa. Nevertheless, no correlation between energy density nor scanning rate can be obtained from the data although for the minimum distortion a tendency can be observed. More data should confirm what it has been seen in this sensitivity study.

Conclusions

From this research work it can be concluded the following:

- No optimal voxel mesh size was found due to the existence of internal parameters (energy exposure fraction) that modify the thermal problem and therefore its distortion and residual stress.
- New material data added made possible to simulate heat treatment and get the same pattern of residual stresses as many research shows: The top layer and the bottom layer have tensile residual stress profile while the middle region has a compressive residual stress profile.
- In Simufact Additive when the 17-4 PH parts have tensile residual stress their distortion is compressive and vice versa, like the welding rule.
- There is an effect between manufacturing one single specimen and multiple specimens at the same time. When more specimens are manufactured at the same time the residual stresses are closer to zero due to less thermal gradient.
- In the sensitivity study, scan speed and beam width affect the energy input (energy density) in the mechanical simulations and have been proved to have an important correlation on the residual stresses, the higher the energy input the more tensile the residual stresses become. The parameters also modify the scan rate which is a term included the energy density.

This project has proved that Simufact Additive is a powerful tool to simulate and obtain residual stresses although the results obtained were distant from the real specimens measured. However, the program can be useful to get a qualitative outcome about the influence of the parameters. For further research, as it has been seen the simulation results were not the same as the measured in the specimens. In this case the research about finding a parameter that describes the real energy input to the layer should be done and could made possible to obtain accurate results. In addition, the thermal treatment was not as the expected with multiple specimens, an investigation about how the thermal treatment works and the right cooling rates also should be conducted. Also, a better understanding of the effect of the energy exposure fraction in the simulation should be done. Finally, as an extra, more material data could be added to get more accuracy and validate completely the model.

Bibliography

- [1] D. Herzog, V. Seyda, E. Wycisk, and C. Emmelmann, "Additive manufacturing of metals," *Acta Mater.*, vol. 117, pp. 371–392, 2016.
- [2] S. L. Sing *et al.*, "Review of selective laser melting: Materials and applications," *Appl. Phys. Rev.*, vol. 2, no. 4, p. 041101, 2015.
- [3] K. Kempen, L. Thijs, B. Vrancken, S. Bols, J. Van Humbeeck, and J.-P. Kruth, "Lowering thermal gradients in selective laser melting by pre-heating the baseplate," 2013.
- [4] M. Brandt, *The role of lasers in additive manufacturing*. Elsevier Ltd, 2016.
- [5] D. Gu *et al.*, "Densification behavior, microstructure evolution, and wear performance of selective laser melting processed commercially pure titanium," *Acta Mater.*, vol. 60, no. 9, pp. 3849–3860, 2012.
- [6] Q. B. Nguyen, D. N. Luu, S. M. L. Nai, Z. Zhu, Z. Chen, and J. Wei, "The role of powder layer thickness on the quality of SLM printed parts," *Arch. Civ. Mech. Eng.*, vol. 18, no. 3, pp. 948–955, 2018.
- [7] V. S. Sufiiarov, A. A. Popovich, E. V. Borisov, I. A. Polozov, D. V. Masaylo, and A. V. Orlov, "The Effect of Layer Thickness at Selective Laser Melting," *Procedia Eng.*, vol. 174, pp. 126–134, 2017.
- [8] B. Zhang, Y. Li, and Q. Bai, "Defect Formation Mechanisms in Selective Laser Melting: A Review," *Chinese J. Mech. Eng. (English Ed.)*, vol. 30, no. 3, pp. 515–527, 2017.
- [9] S. M. Yusuf and N. Gao, "Influence of energy density on metallurgy and properties in metal additive manufacturing," *Mater. Sci. Technol. (United Kingdom)*, vol. 33, no. 11, pp. 1269–1289, 2017.
- [10] Z. Xiang, M. Yin, G. Dong, X. Mei, and G. Yin, "Modeling of the thermal physical process and study on the reliability of linear energy density for selective laser melting," *Results Phys.*, vol. 9, no. February, pp. 939–946, 2018.
- [11] H. K. Rafi, D. Pal, N. Patil, T. L. Starr, and B. E. Stucker, "Microstructure and Mechanical Behavior of 17-4 Precipitation Hardenable Steel Processed by Selective Laser Melting," *J. Mater. Eng. Perform.*, vol. 23, no. 12, pp. 4421–4428, 2014.
- [12] K. G. Prashanth, S. Scudino, T. Maity, J. Das, and J. Eckert, "Is the energy density a reliable parameter for materials synthesis by selective laser melting?," *Mater. Res. Lett.*, vol. 5, no. 6, pp. 386–390, 2017.
- [13] J. P. Kruth, P. Mercelis, J. Van Vaerenbergh, L. Froyen, and M. Rombouts, *Binding mechanisms in selective laser sintering and selective laser melting*, vol. 11, no. 1. 2005.
- [14] Bette, *Fabrication, Applications Engineering in: The Welding Engineer's Current Knowledge*. Duisburg GmbH Germany, 1999.

- [15] J. L. Bartlett and X. Li, "An overview of residual stresses in metal powder bed fusion," *Addit. Manuf.*, vol. 27, no. March, pp. 131–149, 2019.
- [16] P. J. Withers and H. K. D. H. Bhadeshia, "Residual stress part 1 - Measurement techniques," *Mater. Sci. Technol.*, vol. 17, no. 4, pp. 355–365, 2001.
- [17] F. A. Kandil, J. D. Lord, A. T. Fry, and P. V. Grant, "Review of Residual Stress Measurement Methods -A Guide to Technique Selection," *Crown*, vol. 1, no. January 2001, p. 45, 2001.
- [18] P. Mercelis and J. P. Kruth, "Residual stresses in selective laser sintering and selective laser melting," *Rapid Prototyp. J.*, vol. 12, no. 5, pp. 254–265, 2006.
- [19] C. Li, Z. Y. Liu, X. Y. Fang, and Y. B. Guo, "Residual Stress in Metal Additive Manufacturing," *Procedia CIRP*, vol. 71, pp. 348–353, 2018.
- [20] B. Vrancken, R. Wauthle, J.-P. Kruth, and J. Van Humbeeck, "Study of the Influence of Material Properties on Residual Stress in Selective Laser Melting," *Proc. 24th Int. Solid Free. Fabr. Symp.*, pp. 393–407, 2013.
- [21] Y. Liu, Y. Yang, and D. Wang, "A study on the residual stress during selective laser melting (SLM) of metallic powder," *Int. J. Adv. Manuf. Technol.*, vol. 87, no. 1–4, pp. 647–656, 2016.
- [22] A. S. Wu, D. W. Brown, M. Kumar, G. F. Gallegos, and W. E. King, "An Experimental Investigation into Additive Manufacturing-Induced Residual Stresses in 316L Stainless Steel," *Metall. Mater. Trans. A Phys. Metall. Mater. Sci.*, vol. 45, no. 13, pp. 6260–6270, 2014.
- [23] L. S. Anderson, A. M. Venter, B. Vrancken, D. Marais, and J. Van Humbeeck, "Investigating the Residual Stress Distribution in Selective Laser Melting Produced Ti-6Al-4V using Neutron Diffraction," *Mech. Stress Eval. by Neutron Synchrotron Radiat.*, vol. 4, pp. 73–78, 2018.
- [24] L. Parry, I. A. Ashcroft, and R. D. Wildman, "Understanding the effect of laser scan strategy on residual stress in selective laser melting through thermo-mechanical simulation," *Addit. Manuf.*, vol. 12, pp. 1–15, 2016.
- [25] ME 330 Engineering Materials, "Applications and Processing of Metal Alloys: Thermal Processing of Metals," vol. University of Illinois, Illinois, p. , 2016.
- [26] T. LeBrun, T. Nakamoto, K. Horikawa, and H. Kobayashi, "Effect of retained austenite on subsequent thermal processing and resultant mechanical properties of selective laser melted 17-4 PH stainless steel," *Mater. Des.*, vol. 81, pp. 44–53, 2015.
- [27] W. E. Luecke and J. A. Slotwinski, "Mechanical Properties of Austenitic Stainless Steel Made by Additive Manufacturing," *J. Res. Natl. Inst. Stand. Technol.*, vol. 119, p. 398, 2014.
- [28] Y. Sun, R. J. Hebert, and M. Aindow, "Effect of heat treatments on microstructural evolution of additively manufactured and wrought 17-4PH stainless steel," *Mater. Des.*, vol. 156, pp. 429–440, 2018.

- [29] T. L. Starr, K. Rafi, B. Stucker, and C. M. Scherzer, "Controlling phase composition in selective laser melted Stainless steel," pp. 1–5, 2012.
- [30] M. Masoomi *et al.*, "Residual stress measurements via neutron diffraction of additive manufactured stainless steel 17-4 PH," *Data Br.*, vol. 13, pp. 408–414, 2017.
- [31] M. Megahed, H.-W. Mindt, N. N'Dri, H. Duan, and O. Desmaison, *Metal additive-manufacturing process and residual stress modeling*, vol. 5, no. 1. Integrating Materials and Manufacturing Innovation, 2016.
- [32] Simufact Engineering GmbH MSC Software Company, "Simufact Additive© Infosheets," 2018.
- [33] B. Schoinochoritis, D. Chantzis, and K. Salonitis, "Simulation of metallic powder bed additive manufacturing processes with the finite element method: A critical review," *Proc. Inst. Mech. Eng. Part B J. Eng. Manuf.*, vol. 231, no. 1, pp. 96–117, 2017.
- [34] Y. Li, K. Zhou, P. Tan, S. B. Tor, C. K. Chua, and K. F. Leong, "Modeling temperature and residual stress fields in selective laser melting," *Int. J. Mech. Sci.*, vol. 136, no. August 2017, pp. 24–35, 2018.
- [35] H. Mirzadeh, J. M. Cabrera, and A. Najafizadeh, "Constitutive relationships for hot deformation of austenite," *Acta Mater.*, vol. 59, no. 16, pp. 6441–6448, 2011.
- [36] H. J. Rack, "Physical and mechanical properties of Cast 17-4 PH Stainless steel," 1981.
- [37] G. Benghalia and J. Wood, "Material and residual stress considerations associated with the autofrettage of weld clad components," *Int. J. Press. Vessel. Pip.*, vol. 139–140, no. June, pp. 146–158, 2016.